10-24-94 DSD

SANDIA REPORT

SAND94—1498 • UC—405
Unlimited Release
Printed October 1994

CTH Analyses of Steel Rod Penetration into Aluminum and Concrete Targets with Comparisons to Experimental Data

L. N. Kmetyk, P. Yarrington

Prepared by
Sandia National Laboratories
Albuquerque, New Mexico 87185 and Livermore, California 94550
for the United States Department of Energy
under Contract DE-AC04-94AL85000

Approved for public release; distribution is unlimited.

Issued by Sandia National Laboratories, operated for the United States Department of Energy by Sandia Corporation.

Available to DOE and DOE contractors from
Office of Scientific and Technical Information
PO Box 62
Oak Ridge, TN 37831

Prices available from (615) 576-8401, FTS 626-8401

Available to the public from
National Technical Information Service
US Department of Commerce
5285 Port Royal Rd
Springfield, VA 22161

NTIS price codes
Printed copy: A04
Microfiche copy: A01

Distribution
Category UC-405

SAND94-1498
Unlimited Distribution
Printed XXXX 1994

CTH Analyses of Steel Rod Penetration into Aluminum and Concrete Targets with Comparisons to Experimental Data

L. N. Kmetyk
Thermal/Hydraulic Analysis Department
P. Yarrington
Computational Physics and Mechanics Department
Sandia National Laboratories
Albuquerque, NM 87185

Abstract

Calculational results are presented here for a class of intermediate-velocity penetration problems. The problems of interest involve penetration of moderate-strength target materials by high-strength projectiles. Two series of metal penetration experiments and a series of concrete slab perforation tests were simulated in this study. The computer code used for the calculations was the CTH code, which employs a recently-developed "boundary layer" algorithm for treating penetration problems such as these.

Contents

List of Figures

List of Tables

1 Introduction

The calculations presented here were done as part of a calculational benchmarking study to evaluate the capability of current calculational methods for predicting effects associated with penetration of low-strength targets by high-strength projectiles, in a velocity regime where the penetrator remains essentially elastic. As an initial benchmarking activity under this program, two series of metal penetration experiments and a series of concrete slab perforation tests were simulated. The metal penetration problems involved high-strength steel projectiles with two different nose geometries impacting thick cylindrical targets of relatively soft aluminum alloys. The concrete perforation problems again involved high-strength steel projectiles, with the targets in this case being slabs of unreinforced concrete.

The computer code used for the calculations was the CTH [1] code, which was developed to treat a wide range of continuum dynamics problems involving intense, impulsive loading of materials. The calculations used a relatively new "boundary layer algorithm" [2, 3] in CTH to treat the interface between penetrator and target. This algorithm eliminates the artificial erosion of penetrator material that can occur in Eulerian code calculations.

The work presented here involves CTH simulations of the following problems:

1. penetration of aluminum targets by steel ogival-nosed rods [4] (Section 2),
2. penetration of aluminum targets by steel hemispherical-nosed rods [5] (Section 3),
3. penetration of concrete targets by steel ogival-nosed rods [6] (Section 4).

Each section includes a brief description of the experiments, the CTH input model and parameters used, and comparisons of calculational results to the test data. Overall conclusions are summarized in Section 5.

2 Penetration of Aluminum Targets by Ogival-Nosed Steel Rods

2.1 Experiment Description

Forrestal *et al.* [4] conducted terminal-ballistic experiments involving 0.711cm-diameter, 25gm, 3.0 caliber-radius-head (CRH), ogival-nosed steel rods of length $L = 7.112$cm impacting 7075-T651 aluminum cylindrical targets.

The projectile shape is shown in Figure 2.1.1. Projectiles were T-200 maraging steel with density $\rho_p = 8.02$gm/cc and a nominal yield stress of 1.72GPa. The range of impact velocities was between 370 and 1260m/s, as indicated in Table 2.1.1. Impact was normal to within 2^o.

The targets were cut from 15.2cm-diameter bars, wbp the target length for each test is given in Table 2.1.1. In addition, axial specimens of this bar stock were machined for large-strain compression tests. Figure 2.1.2 shows data for compression tests at a strain rate of 10^{-1}/s, along with a power law data fit discussed in Ref. [4].

For the projectile impact experiments, post-test penetration depths were measured from in-material X-ray photographs, with results summarized in Table 2.1.1.

2.2 CTH Model Input

The CTH calculations were performed using 2D cylindrical coordinates. Figure 2.2.1. shows CTH material plots of the initial condition for these calculations.

Most of the calculations were performed with a basecase zoning of 75×825 cells. The x-direction mesh was started at x = 0, the axis of symmetry, and extended to a radius of 1.0cm using 25 uniform cells of 0.04cm width. (Recall that the rod outer radius was 0.3555cm.) This was followed by 50 more cells of increasing (at ~5% rate) size in the x-direction to an outer radius of ~8.5cm to cover the entire target. In the y-direction, the mesh was started at y = -24cm, wbp y = 0 was taken as the impact surface of the target, and the bottom of the cylindrical target was at y = -22.9cm. The mesh extended to +9cm in the y-direction using 825 uniform cells of 0.04cm width. Thus, a subgrid of square cells covered the penetration region, with the cell size being 0.04cm in both the x- and y-directions.

The various material properties used in the CTH calculations for these tests are given in Table 2.2.1. Both the penetrator and the target were modelled with analytic Mie-Gruneisen equations of state. The penetrator was modelled as an elastic-perfectly plastic material. The aluminum target was modelled using the Johnson-Cook viscoplastic model [7], with material constants based on a fit to the data shown in Figure 2.1.2 for 7075-T651 aluminum.

The density and yield strength of the steel were increased by a factor

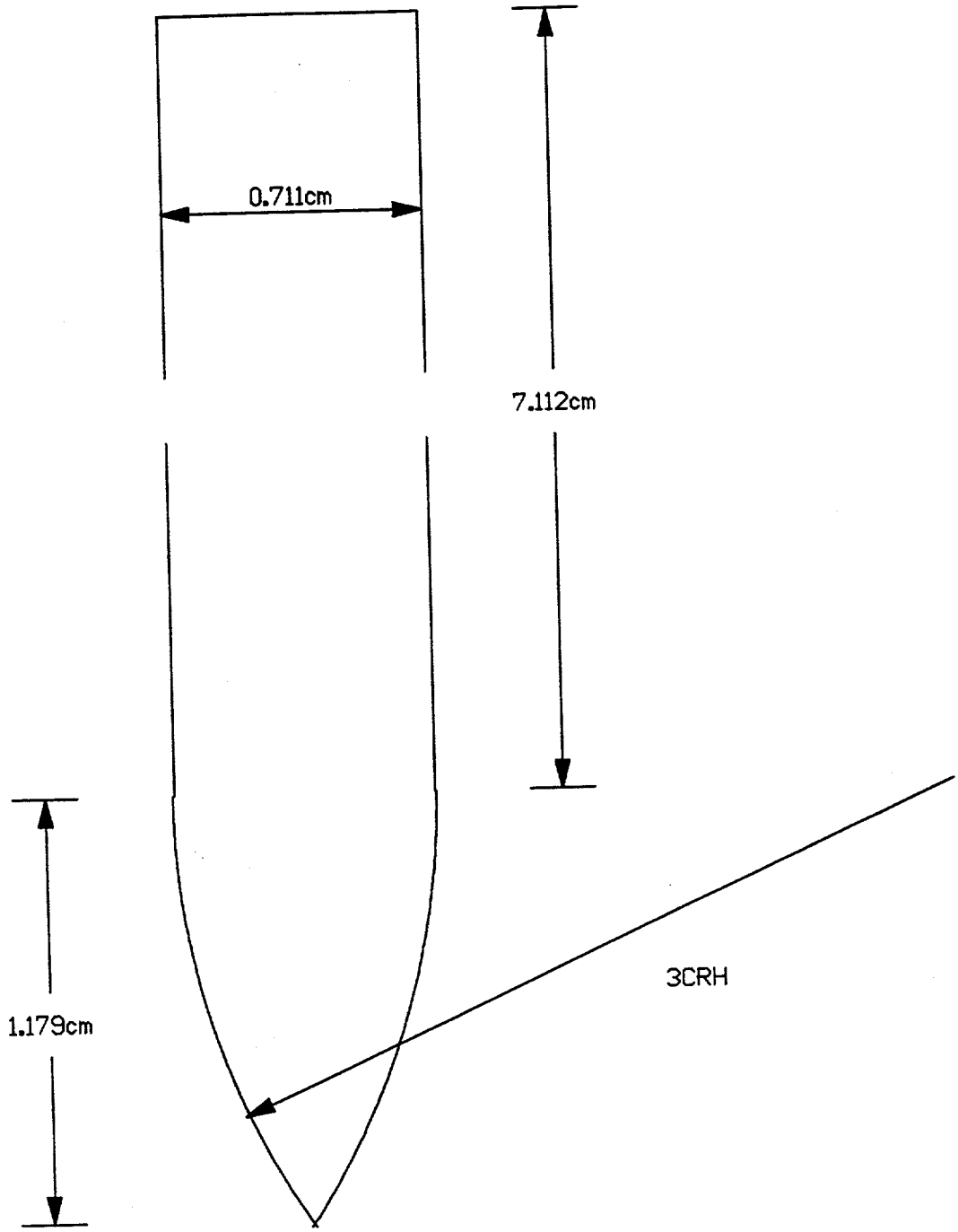

Figure 2.1.1. Projectile Geometry – Ogival-Nosed Rod for 7075-T651 Aluminum Target Tests

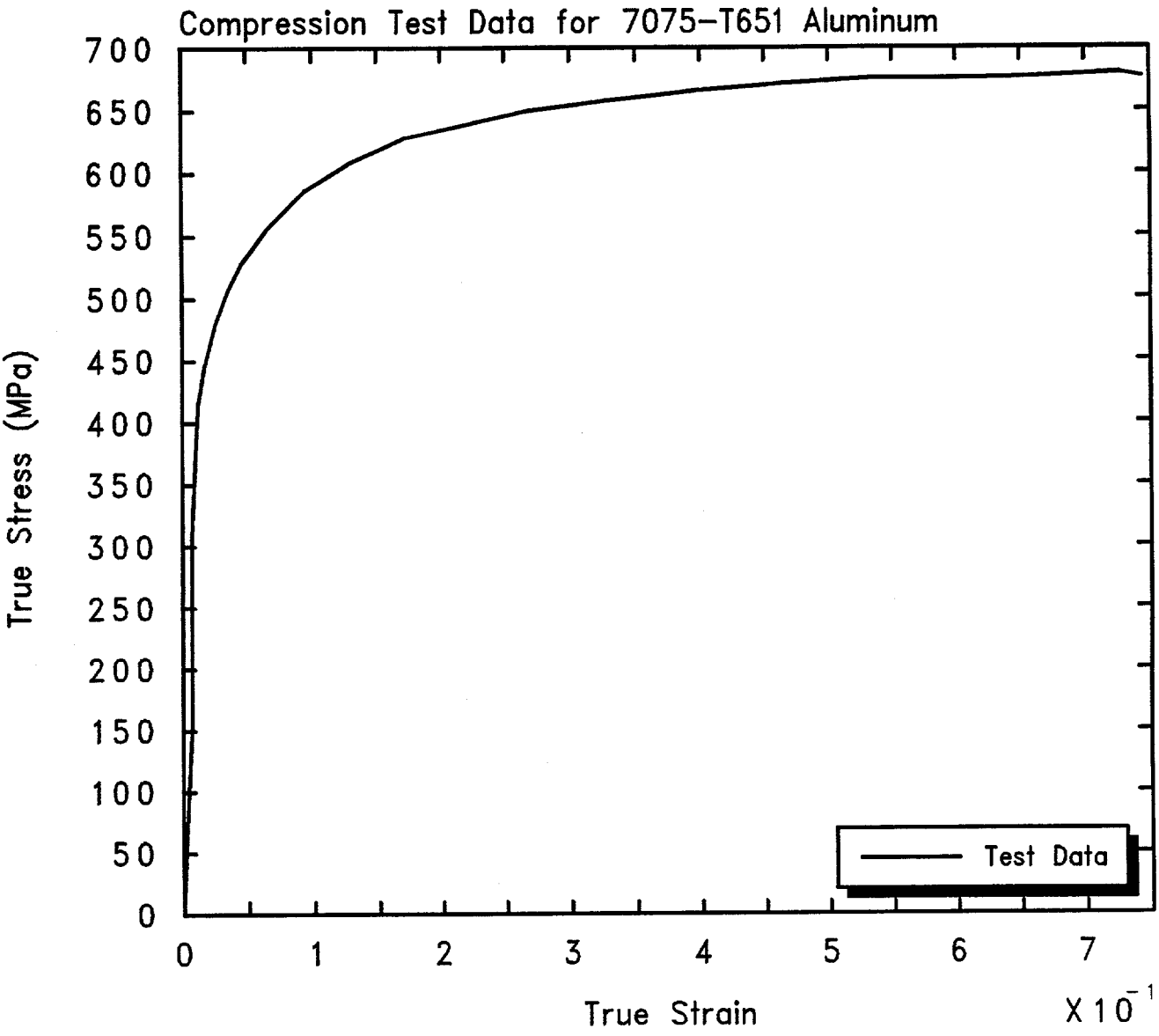

Figure 2.1.2. Compression Stress-Strain Curves for the 7075-T651 Aluminum Target Material

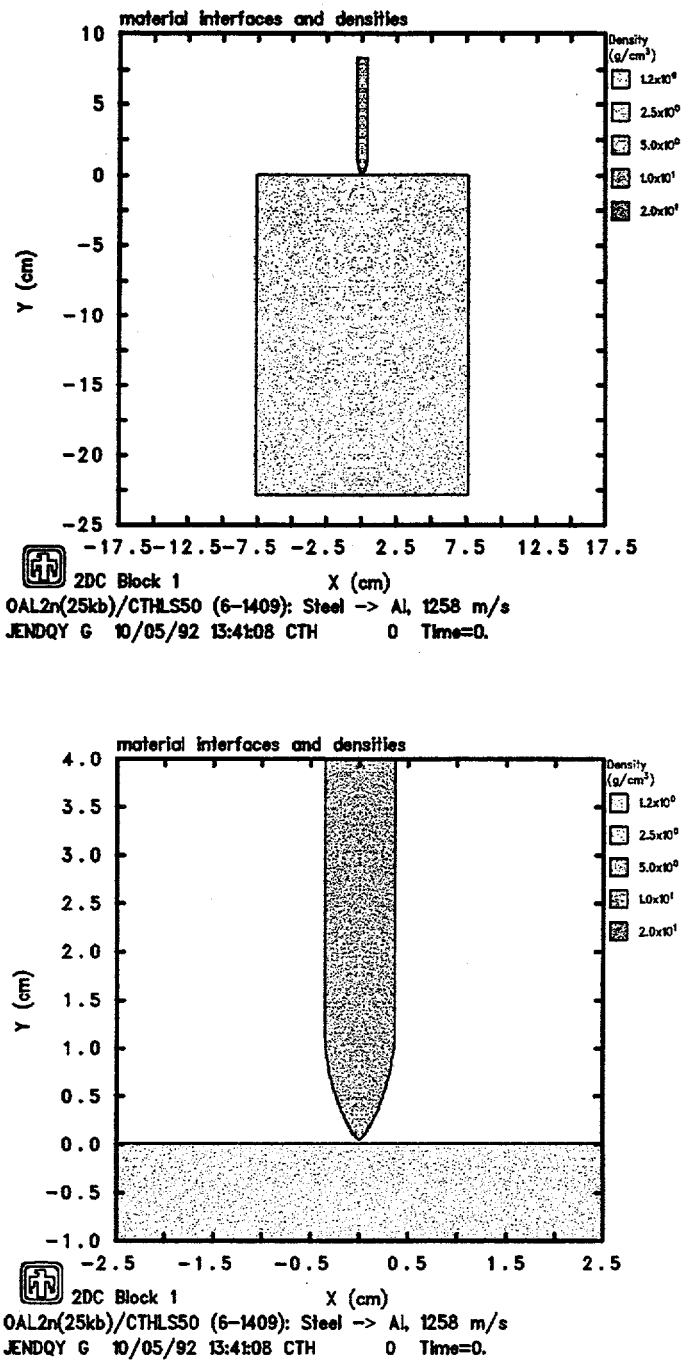

Figure 2.2.1. Initial Configuration for CTH Analyses – Ogival-Nosed Rods Penetrating 7075-T651 Aluminum Targets

$$\left(\frac{(r_o + w_{sl}/2)}{r_o}\right)^2$$

to account for boundary layer effects, wbp r_o is the penetrator outer radius and w_{sl} is the slip layer thickness. (This correction can be made automatically as an option in the boundary layer algorithm input [2].) Both the boundary layer thickness, w_{bl}, and the slip layer thickness, w_{sl}, were specified to be 0.08cm, *i.e.*, twice the zone size in the projectile/target interaction region.

The penetration calculations were performed with the nonequilibrium, multi-material temperature and multi-material pressure modelling options in CTH, with the high-resolution interface tracker. Velocity was specified to be convected conserving momentum exactly and discarding any kinetic energy discrepancies. Artificial viscosity was used, with default values for the linear and quadratic coefficients, and the shear artificial viscosity increased to 0.1. The region around the penetrator and target was modelled as void.

2.3 Calculational Results

Calculations were run for the five different values of impact velocity listed in Table 2.1.1. Results of calculations with $\Delta x = \Delta y = 0.04$ in the penetration region and $w_{bl} = w_{sl} = 0.08$ are shown in Figure 2.3.1. This plot gives penetration depth as a function of impact velocity. The experimental data [4] are also shown. Both the calculational results and the experimental data are represented by plot symbols, with straight-line segments connecting the symbols to highlight overall trends.

Figure 2.3.1 also shows the effect of varying the friction coefficient f between 0.0 and 0.12. In general, the calculations predict somewhat deeper penetration depths than were observed in the tests.

Figure 2.3.2 illustrates the predicted shape of the penetrator and cavity at 400μs, when the penetrator has come to a full stop for an impact velocity of 1258m/s. Note that the penetrator shows essentially no permanent deformation, which is consistent with the test observations [4].

Axial stress contours predicted at four different times during the penetration process are depicted in Figure 2.3.3. The contours show an essentially steady-state stress distribution on the penetrator developing after a few noselengths of penentration.

Figure 2.3.4 presents the rigid-body decelerations calculated for these tests as a function of both velocity, in the upper plot, and depth of penetration, in the lower plot. (The rigid-body decelerations plotted in this report are the time derivatives of the mass-weighted average velocity of the penetrator material, smoothed using a bell-shaped function with a 0.05ms time constant.) For the higher impact velocities above ~400m/s, the decelerations all fall on the same deceleration *vs* velocity curve and reach a reasonably

Table 2.1.1. Data Summary – Ogival-Nosed Rods and 7075-T651 Aluminum Target Tests

Shot number	Mass (gm)	V_0 (m/s)	α† (degrees)	β† (degrees)	P‡ (cm)	Target length (cm)
6-1397	24.8	372	0.4	0.8	2.6	12.7
6-1398	24.7	695	1.9	1.7	7.0	12.7
6-1391	24.8	978	0	0	12.7	17.8
6-1402	24.7	1067	0.1	0.7	14.7	22.9
6-1409	24.8	1258	1.3	1.1	20.9	22.9

†α and β are pitch and yaw angles, respectively
‡P is penetration depth to nose tip from original target impact surface

Table 2.2.1. Material Properties Used in CTH Analyses for Ogival-Nosed Rods Penetrating 7075-T651 Aluminum Targets

Property	Penetrator (Steel)	Target (Aluminum)
Density, ρ (gm/cm^3)	8.02	2.70
Sound speed, C_S (cm/s)	4.610×10^5	5.380×10^5
$U_s - U_p$ slope, S	1.73	1.337
Gruneisen coefficient, Γ	1.67	2.100
Specific heat, C_V (erg/gm-eV)	5.34×10^{10}	1.02×10^{11}
Poisson's ratio, ν	0.3	0.33
Yield stress, Y (dynes/cm^2)	17.2×10^9	
Johnson-Cook model constants		
A (dynes/cm^2)		4.48×10^9
B (dynes/cm^2)		2.95×10^8
C (dynes/cm^2)		0
n		0.39205
T_M (eV)		0.0668
P_{FRAC} (dynes/cm^2)	-35×10^9	-5×10^9

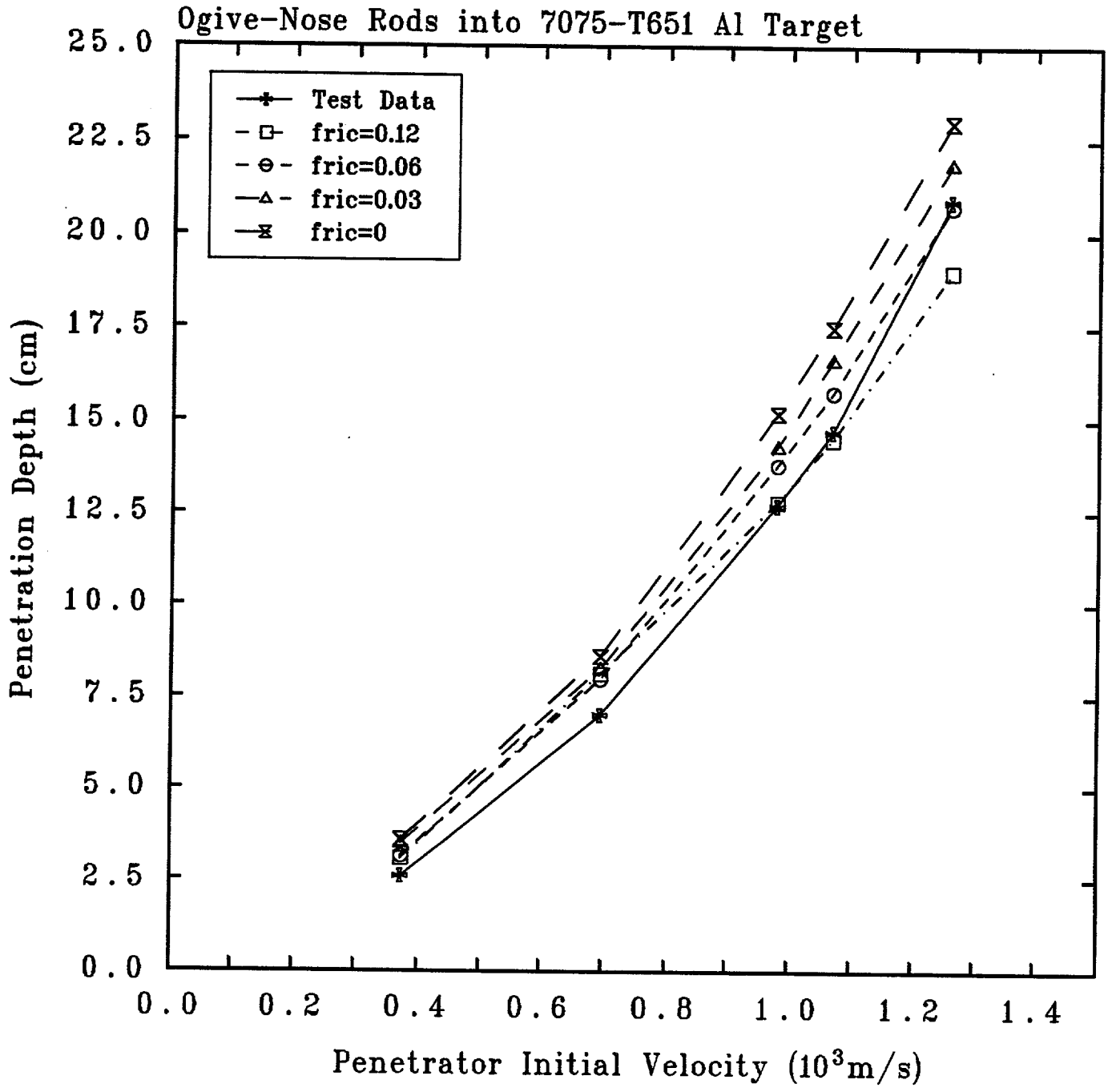

Figure 2.3.1. Penetration Depth *vs* Impact Velocity – Ogival-Nosed Rods Penetrating 7075-T651 Aluminum Targets

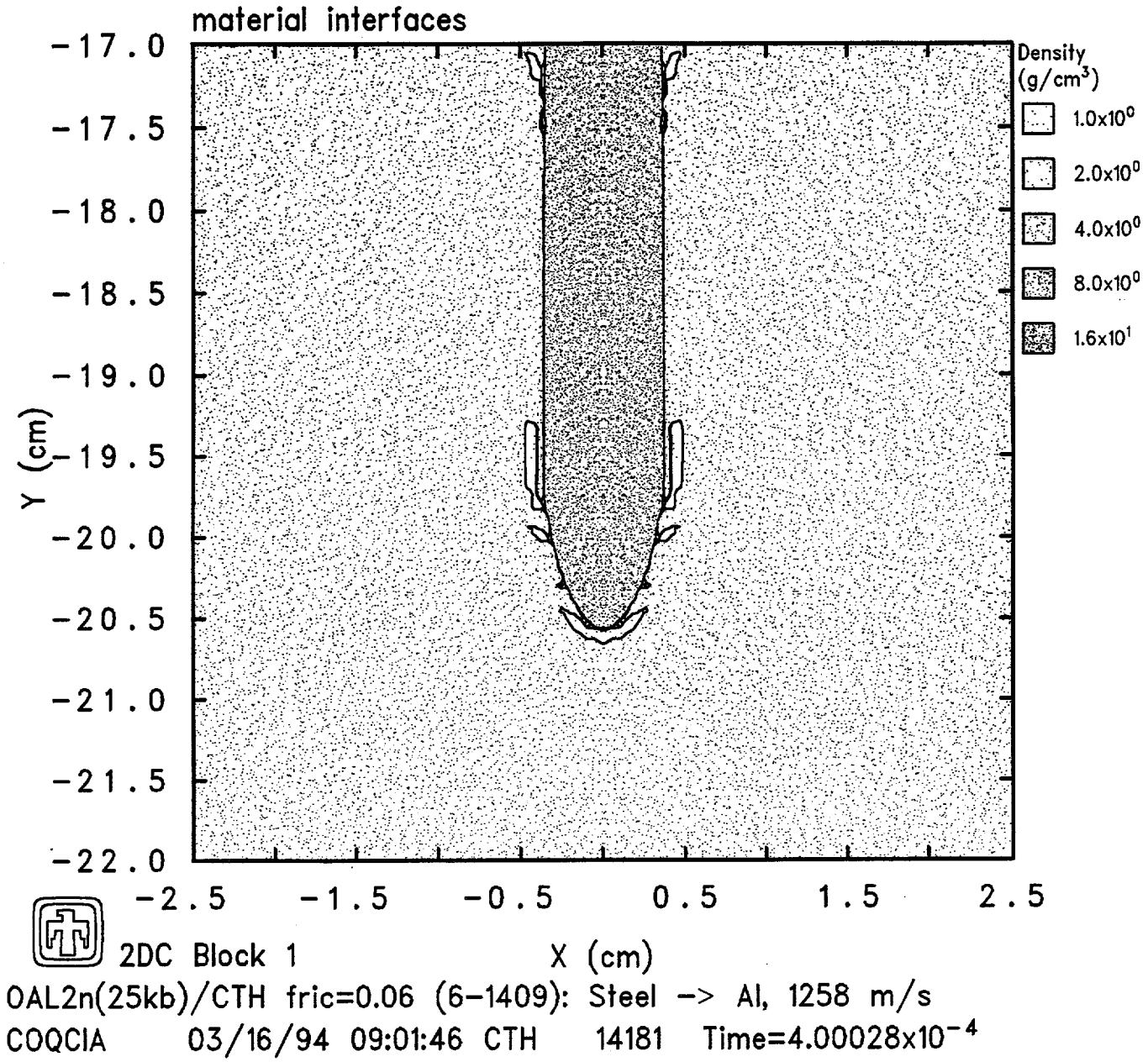

Figure 2.3.2. Predicted Final Configuration for Ogival-Nosed Rod Penetrating 7075-T651 Aluminum Targets at 1258m/s Impact Velocity

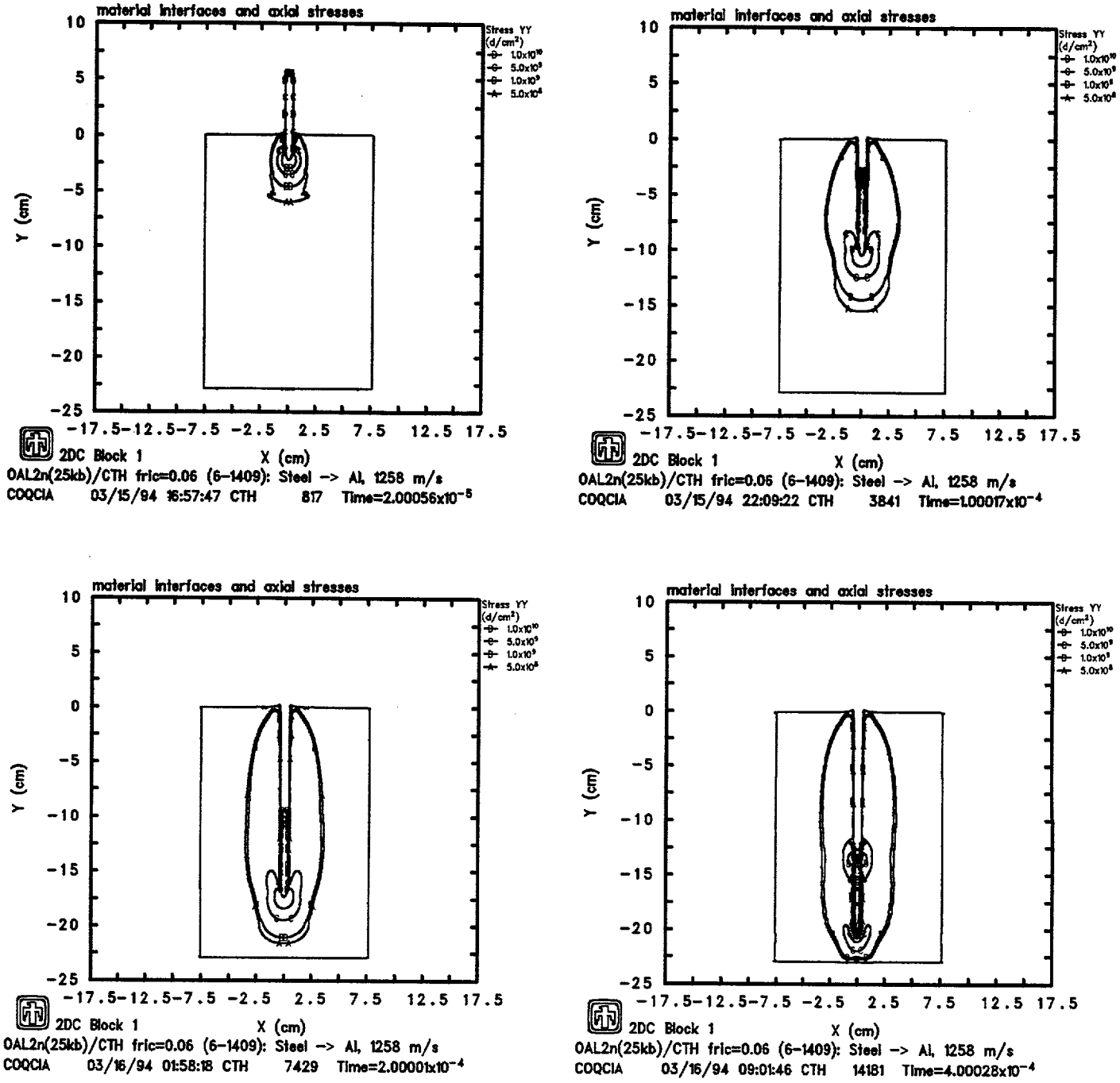

Figure 2.3.3. Axial Stress Contours Predicted by CTH during Penetration for 1258m/s Impact Velocity (A: 0.5kbar, B: 1kbar, C: 5kbar, D: 10kbar) – Ogival-Nosed Rod Penetrating 7075-T651 Aluminum Target

steady-state value of $\sim 4 \times 10^6 \mathrm{m/s^2}$ ($\sim 4 \times 10^5 g$'s) after about four noselengths of penetration. For the impact velocity of 372m/s the penetrator stopped before reaching that steady state level.

The importance and necessity of the boundary layer algorithm [2] in CTH was demonstrated by rerunning one of the calculations without the new model. Calculational results for the 1258m/s impact velocity without the boundary layer algorithm predict less than half the penetration observed in the corresponding experiment. This result highlights the difficulty that an Eulerian code such as CTH can have in correctly predicting penetration of softer targets by nearly-rigid penetrators. The difficulty is due to the effect of materials mixing within cells along the penetrator-target interface. The new CTH boundary-layer algorithm used for the present calculations eliminates the artificial erosion of projectile material in mixed-material cells and allows much more accurate simulation of sliding solid surfaces.

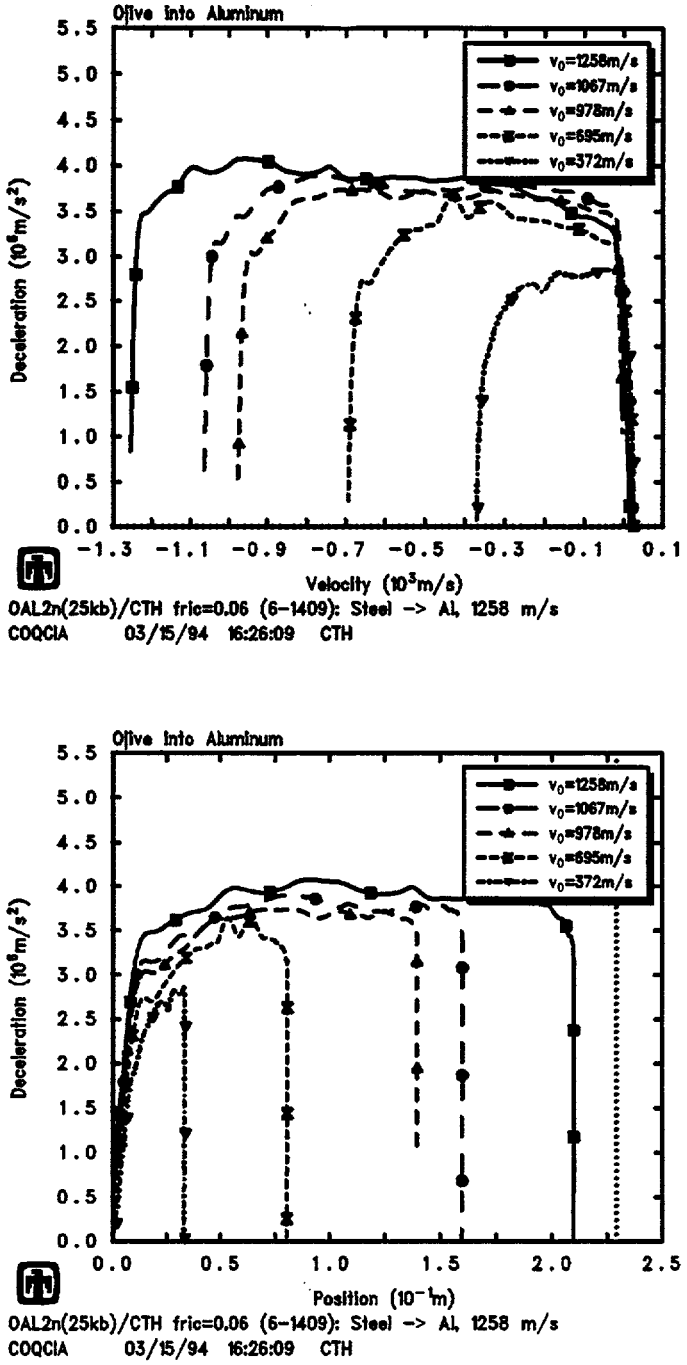

Figure 2.3.4. Rigid-Body Decelerations Predicted by CTH for Various Impact Velocities – Ogival-Nosed Rods Penetrating 7075-T651 Aluminum Targets

3 Penetration of Aluminum Targets by Hemispherical-Nosed Steel Rods

3.1 Experiment Description

A second series of metal penetration experiments was conducted by Forrestal, Brar and Luk [5] using hemispherical-nosed, high-stength steel projectiles and 6061-T651 aluminum targets.

The projectile geometry is shown in Figure 3.1.1. The projectiles in these tests had a diameter of 0.711cm and body length of 7.112cm. Note that overall projectile length was somewhat smaller than the ogival-nosed rods discussed in Section 2, due to the blunter hemispherical geometry of the nose. Projectiles were T-200 maraging steel with a density ρ_p of 8.02gm/cc and a nominal yield stress of 1.72GPa. The range of impact velocities is indicated in Table 3.1.1. Impact was normal to within 3°.

Table 3.1.1. Data Summary – Hemispherical-Nosed Rods and 6061-T651 Aluminum Target Tests

Shot number	Mass (gm)	V_0 (m/s)	α† (degrees)	β† (degrees)	P‡ (cm)	Target length (cm)
2037	23.36	359	0.0	1.2	2.1	9.0
1961	23.34	430	-	0.2	3.2	8.9
1960	23.34	490	-	0.7	4.0	8.2
1916	23.43	519	2.0	2.8	4.1	11.4
1914	23.40	673	0.7	1.0	7.3	17.8
1915	23.44	792	2.6	1.8	8.5	17.8
2059	23.32	959	1.0	0.5	10.9	19.8
1912	23.32	1009	1.0	0.2	12.9	21.6

†α and β are pitch and yaw angles, respectively
‡P is penetration depth to nose tip from original target impact surface

The targets were cut from 15.2cm-diameter bars, where the target length for each test is given in Table 3.1.1. In addition, axial and transverse specimens for this bar stock were machined for large-strain compression tests. Four specimens were tested at a strain rate of 10^{-2}/s, and Figure 3.1.2 shows the compression stress-strain test data, along with a power law fit to the data [5].

Post-test penetration depths were measured from in-material radiographs, with results summarized in Table 3.1.1.

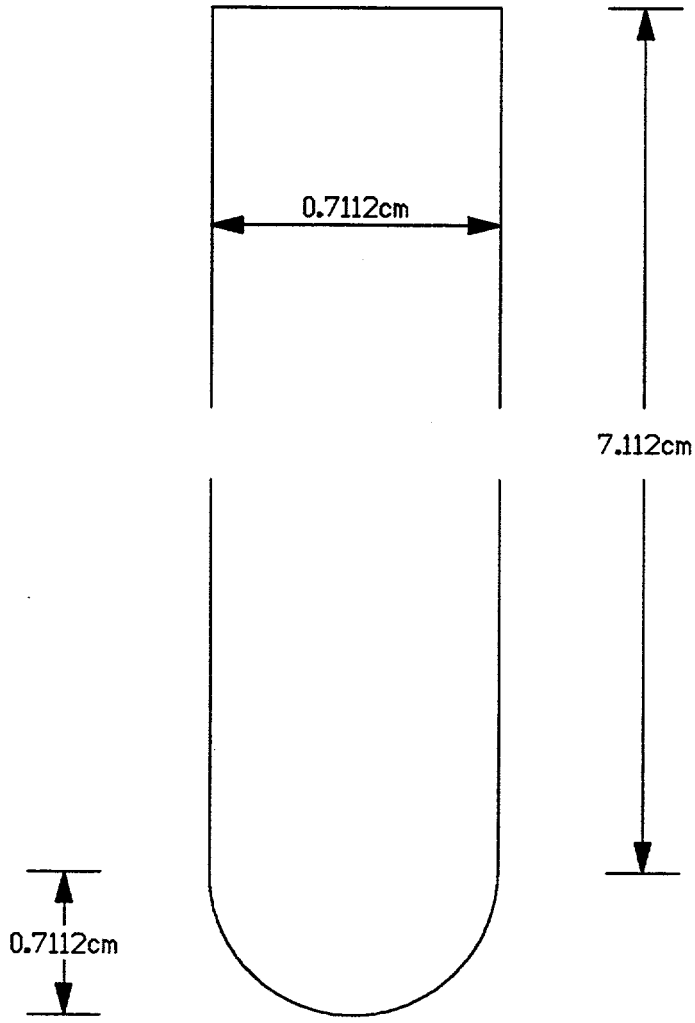

Figure 3.1.1. Projectile Geometry – Hemispherical-Nosed Rod for 6061-T651 Aluminum Target Tests

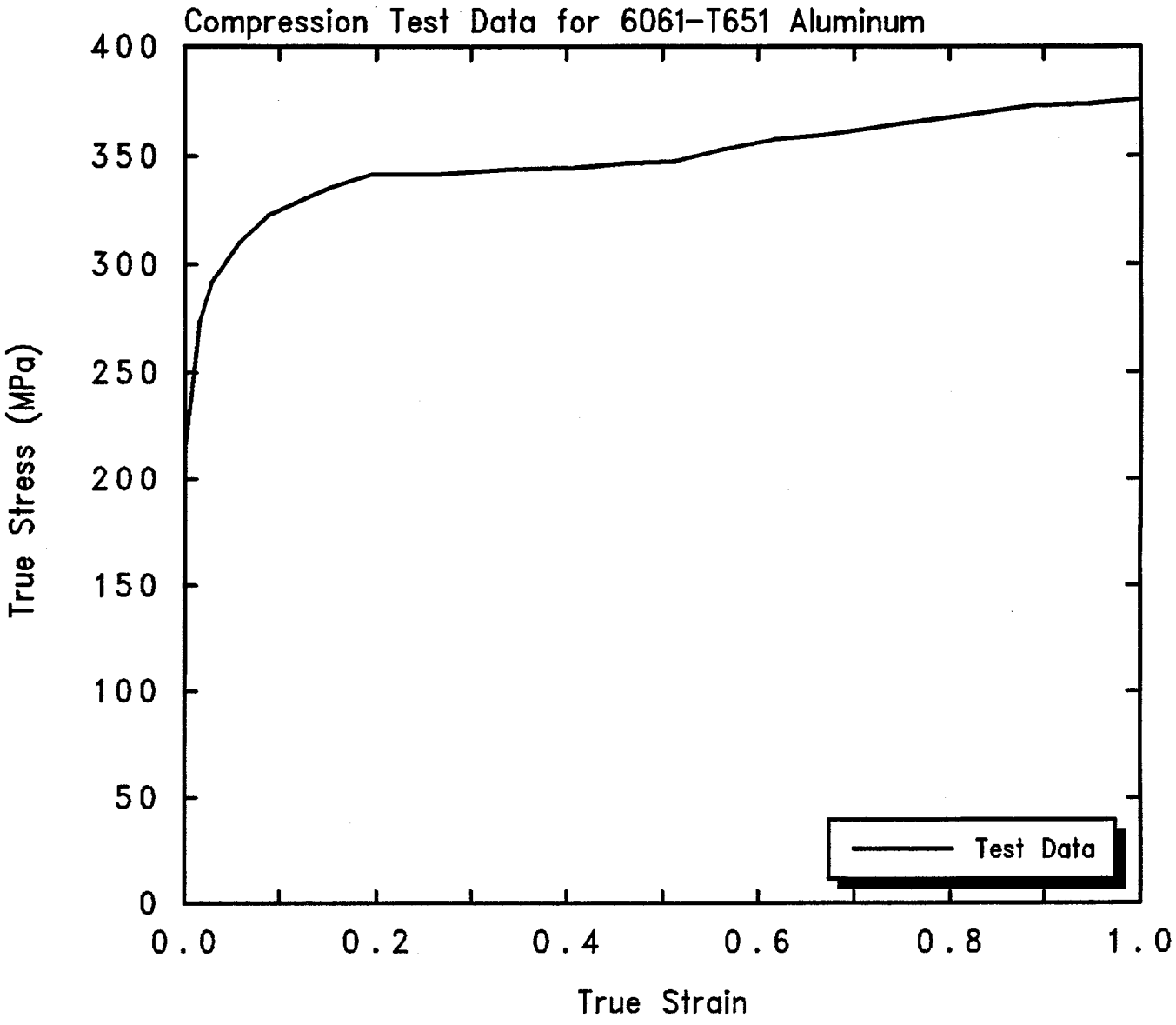

Figure 3.1.2. Stress-Strain Data for the 6061-T651 Target Material

3.2 CTH Model Input

The CTH calculations were performed using 2D cylindrical coordinates and Figure 3.2.1 shows the initial configuration for the calculations.

Most of the calculations were performed with a basecase zoning of 75×750 cells. The x-direction mesh was the same as used in the calculations for the ogival-nosed rods, as discussed in Section 2.2. The slightly smaller rod length and target thickness, however, allowed a small reduction in the extent of the y mesh, so that in the y-direction the mesh was started at y = -22cm. Thus, a subgrid of square cells again covered the penetration region, with the cell size being 0.04cm in both the x- and y-directions.

Table 3.2.1. Material Properties Used in CTH Analyses for Hemispherical-Nosed Rods Penetrating 6061-T651 Aluminum Targets

Property	Penetrator (Steel)	Target (Aluminum)
Density, ρ (gm/cm^3)	8.02	2.70
Sound speed, C_S (cm/s)	4.61×10^5	5.38×10^5
$U_s - U_p$ slope, S	1.73	1.337
Gruneisen coefficient, Γ	1.67	2.100
Specific heat, C_V (erg/gm-eV)	5.34×10^{10}	1.02×10^{11}
Poisson's ratio, ν	0.3	0.33
Yield stress, Y (dynes/cm^2)	17.2×10^9	
Johnson-Cook model constants		
A (dynes/cm^2)		2.76×10^9
B (dynes/cm^2)		0.92×10^9
C (dynes/cm^2)		0
n		0.2591
T_M (eV)		0.0792
P_{FRAC} (dynes/cm^2)	-35×10^9	-5×10^9

The various material properties used in the CTH calculations are given in Table 3.2.1. Both the penetrator and the target were modelled with an analytic Mie-Gruneisen equation of state. The penetrator was modelled as an elastic-perfectly plastic material and the density and yield strength of the steel were increased to account for boundary layer effects (see Section 2.2) . Both the boundary layer thickness, w_{bl}, and the slip layer thickness, w_{sl}, were specified to be 0.08. The aluminum target was modelled using the Johnson-Cook viscoplastic model [7], with material constants based on a fit to the data shown in Figure 3.1.2.

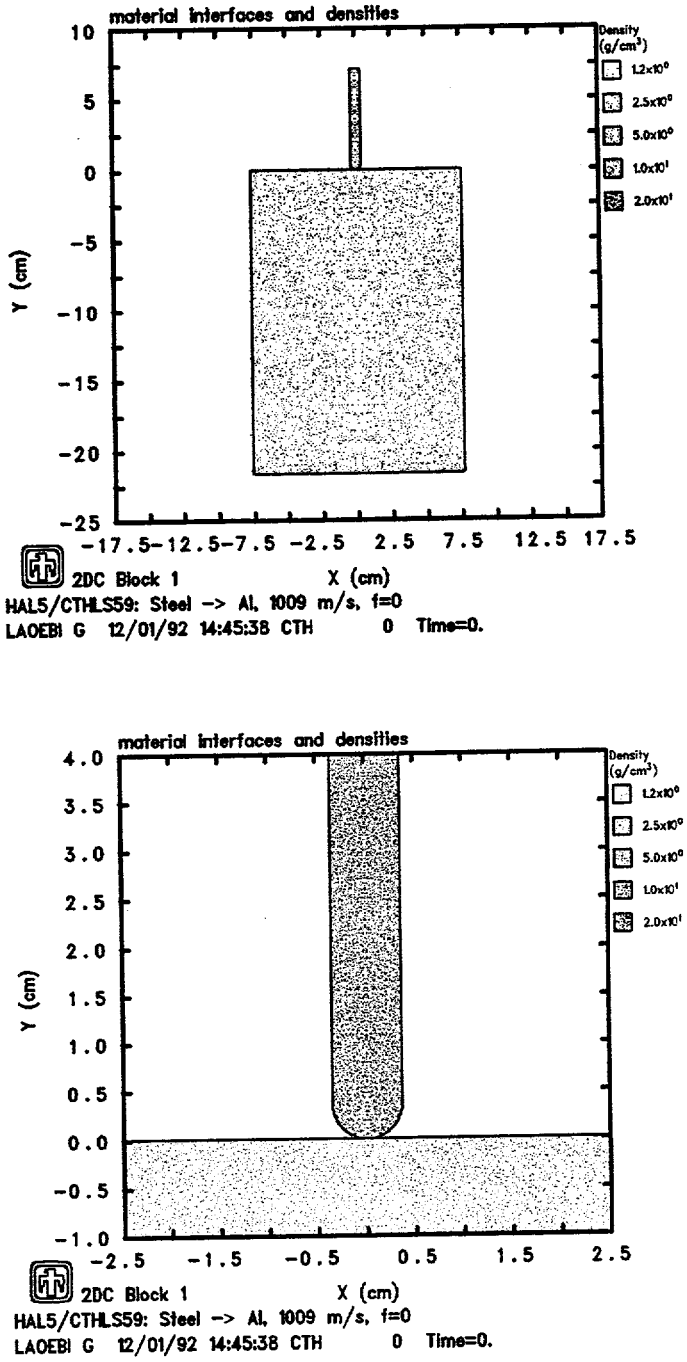

Figure 3.2.1. Initial Configuration for CTH Analyses – Hemispherical-Nosed Rods Penetrating 6061-T651 Aluminum Targets

The calculations were performed with the nonequilibrium, multi-material temperature and multi-material pressure modelling options, with the high-resolution interface tracker, and without the fragment mover option. Velocity was specified to be convected conserving momentum exactly and discarding any kinetic energy discrepancies. Artificial viscosity was used, with default values for the linear and quadratic coefficients, and the shear artificial viscosity increased to 0.1. The region around the penetrator and target was modelled as void.

3.3 Calculational Results

Calculations were run for eight different values of impact velocity, as indicated in Table 3.1.1. Results of calculations with three different friction coefficients (0.0, 0.03 and 0.06) are shown in Figure 3.3.1. This plot gives penetration depth as a function of impact velocity. The experimental data [5] are also shown. Both the calculations and the experimental data are represented by the plot symbols, with straight-line segments connecting the results to highlight trends. There is overall good agreement with the data; however, the experimental data generally lie slightly below the calculational results.

Figure 3.3.2 shows the predicted shape of the penetrator and cavity after the penetrator has come to a full stop, for the case of the 1009m/s impact velocity. Again, both calculation and experiment show little or no permanent deformation of the projectile.

Figure 3.3.3 presents the calculated rigid-body decelerations for various impact velocities, as a function of both velocity, in the upper plot, and depth of penetration, in the lower plot. (The rigid-body decelerations plotted in this report are the time derivatives of the mass-weighted average velocity of the penetrator material, smoothed using a bell-shaped function with a 0.05ms time constant.)

Since the target material was significantly different for the ogival-nosed and hemispherical-nosed penetration tests, differences in penetration depth were not due to differences in nose shape only. To investigate the influence of nose shape on penetrator performance, the nose geometry was changed to hemispherical in one of the 3CRH ogival-nosed rod problems, keeping all other factors the same. The result of this calculation is plotted in Figure 3.3.4 and shows about a factor of two decrease in penetration depth for an equal-mass hemispherical-nosed rod relative to the ogival-nosed rod. The rigid-body decelerations for the ogival-nose rod and for the hemispherical-nosed rod are compared in Figure 3.3.5. The factor of $\sim$2 increase in rigid-body deceleration for the hemispherical-nosed penetrator corresponds to the decrease in penetration depth noted above.

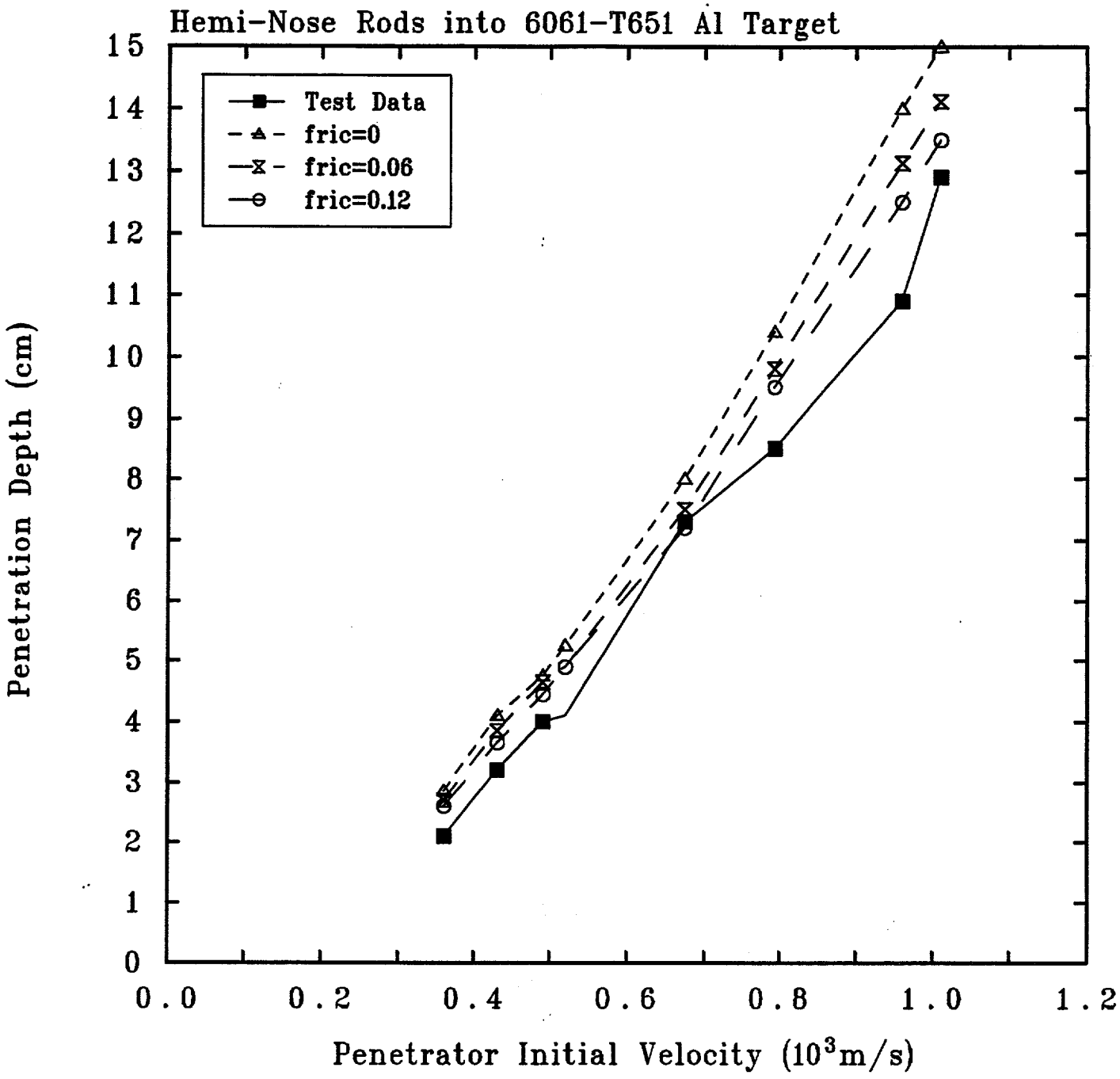

Figure 3.3.1. Penetration Depth Predicted by CTH for Various Impact Velocities and Friction Factors – Hemispherical-Nosed Rods Penetrating 6061-T651 Aluminum Targets

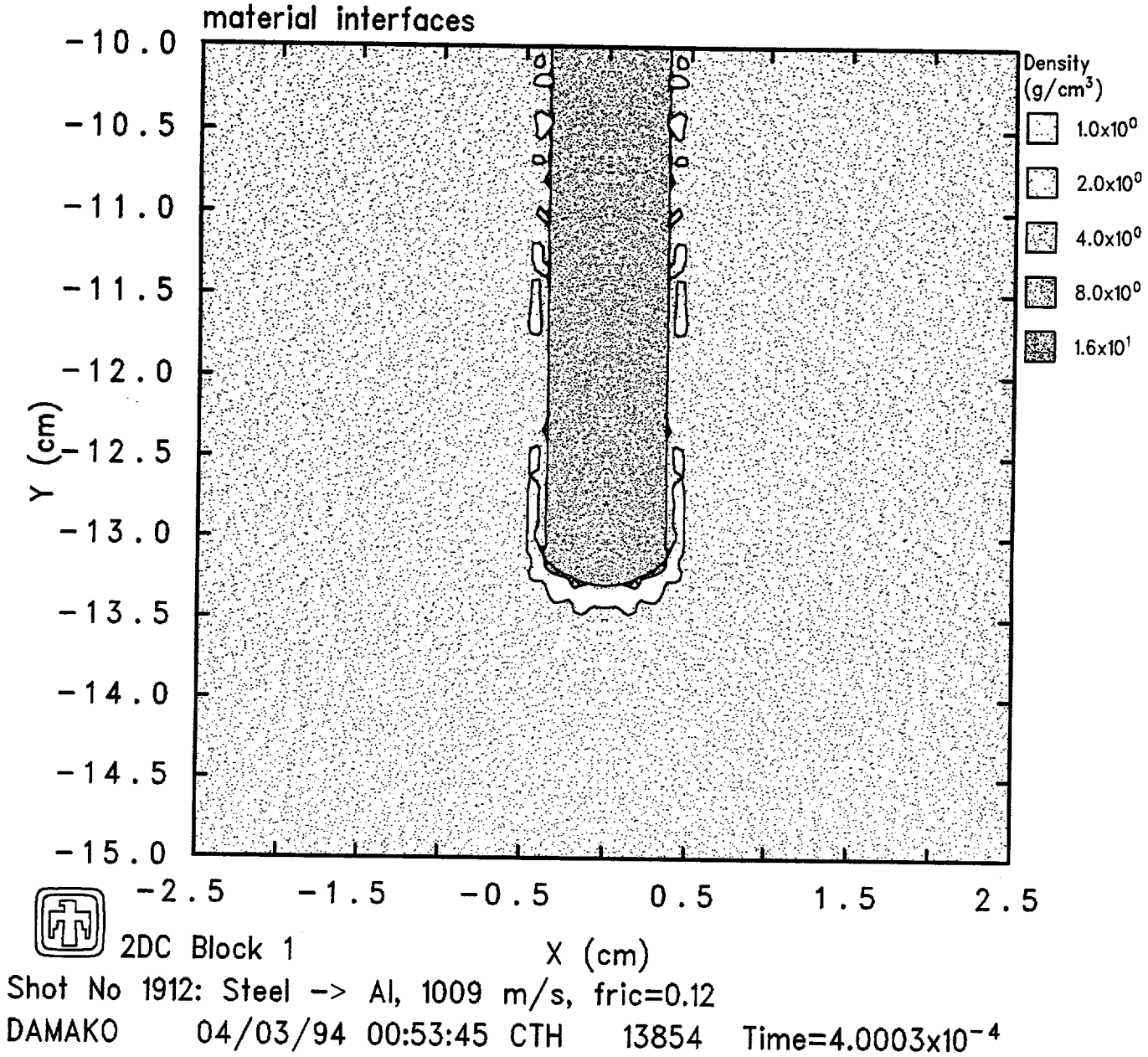

Figure 3.3.2. Final Configuration Predicted by CTH for a Hemispherical-Nosed Rod Penetrating a 6061-T651 Aluminum Target at an Impact Velocity of 1009m/s

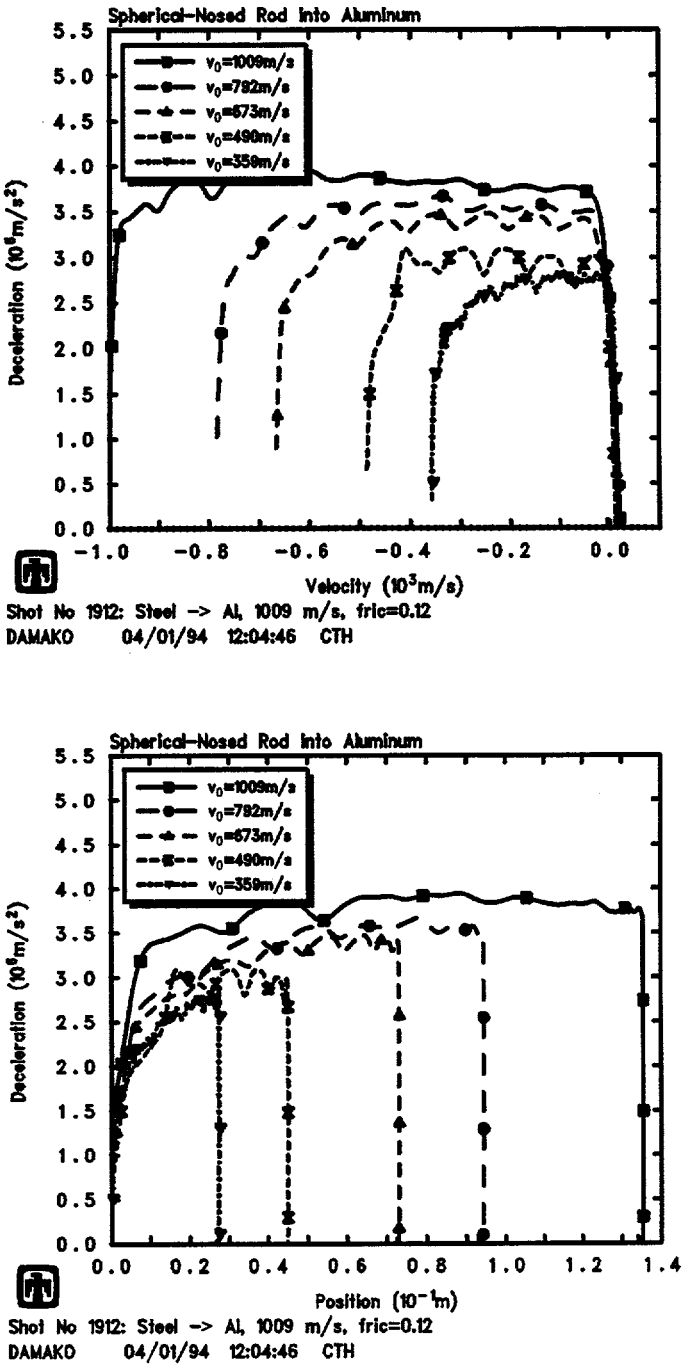

Figure 3.3.3. Rigid-Body Decelerations Predicted by CTH for Various Impact Velocities – Hemispherical-Nosed Rods Penetrating 6061-T651 Aluminum Targets

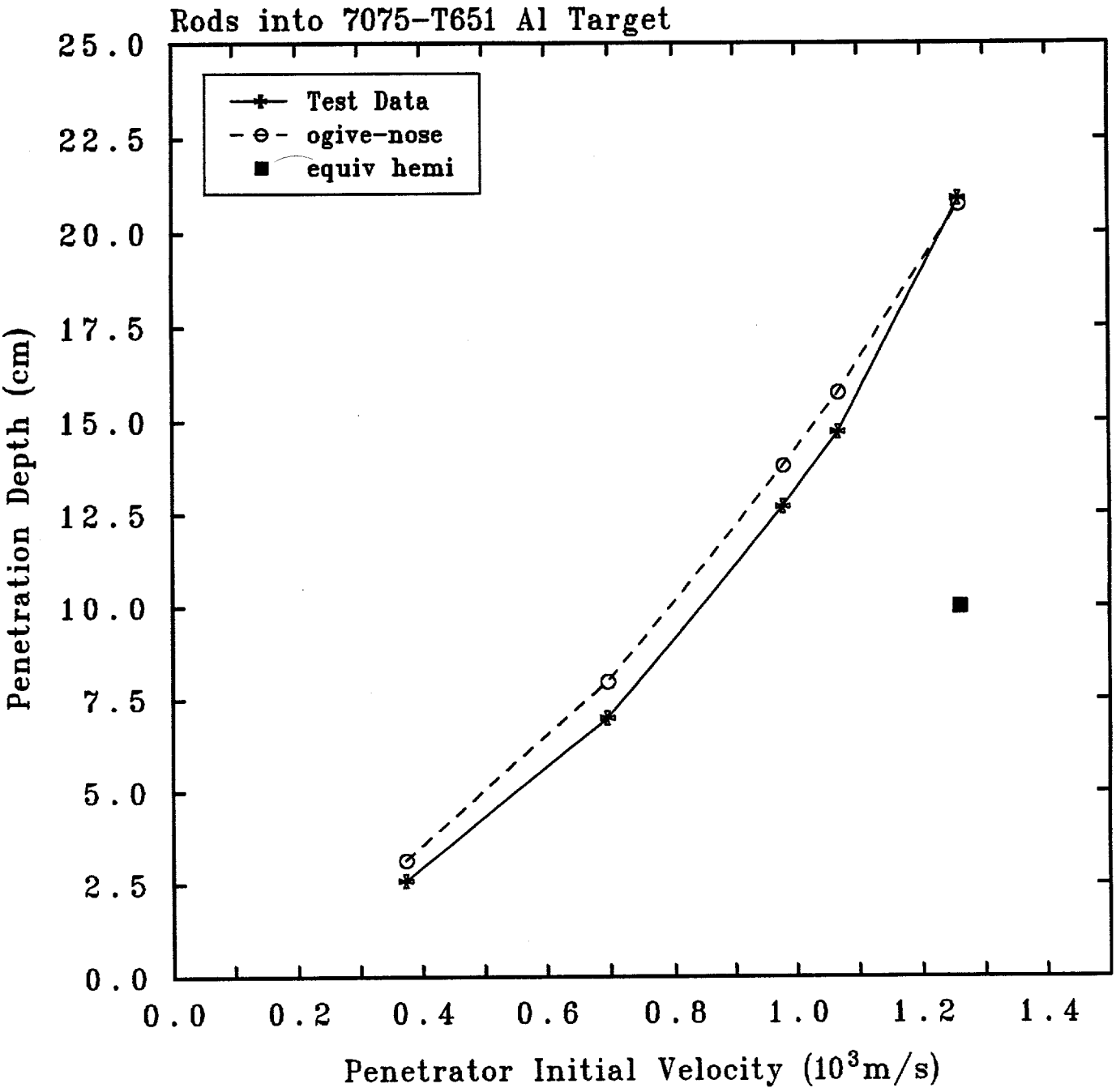

Figure 3.3.4. Penetration Depth Predicted by CTH for Ogival- and Hemispherical-Nosed Rods of Equal Mass Penetrating 7075-T651 Aluminum Targets

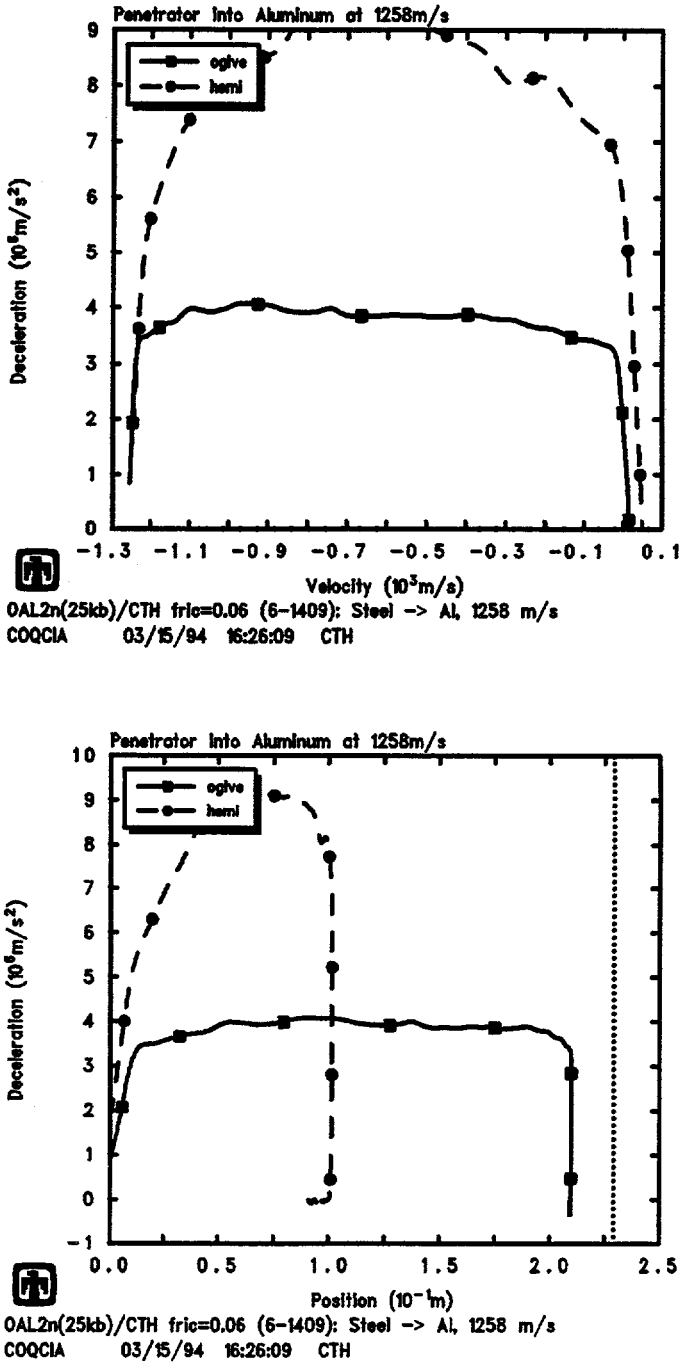

Figure 3.3.5. Rigid-Body Decelerations Predicted by CTH for Ogival- and Hemispherical-Nosed Rods of Equal Mass Penetrating 7075-T651 Aluminum Targets at 1258m/s Impact Velocity

4 Penetration of Concrete Targets by Ogival-Nosed Steel Rods

4.1 Experiment Description

Hanchak *et al.* [6] conducted perforation experiments with 500gm, 3CRH ogival-nosed rods into concrete slabs with 48MPa and 140MPa unconfined compressive strengths. The present calculations modelled only the tests in the high-strength material.

The projectile shape is shown in Figure 4.1.1, with a rod diameter of 2.54cm, a rod length of 10.16cm, and a nose length of 4.21cm. Projectiles were machined of T-250 maraging steel with density $\rho_p = 8.02$gm/cc and a nominal yield stress of 1.72MPa. The range of impact velocities was between 300 and 1100m/s, as given in Table 4.1.1. Impact was normal to within 3°.

Residual velocities given in Table 4.1.1 were measured with flash radiographs, which also showed that the projectiles were not fractured by the targets. Recovered projectiles showed only minor nose erosion.

Table 4.1.1. Data Summary – Ogival-Nosed Rods and 140MPa Concrete Target Tests

Shot number	V_0 (m/s)	V_r (m/s)	Pitch (degrees)	Yaw (degrees)
1-0062	376	0	0	2.5
1-0061	382	0	0	2.0
1-0057	443	171	0	0
1-0066	522	265	1.5	1.5
1-0065	587	368	1.0	1.0
1-0055	743	544	2.0	0
1-0067	998	842	0	1.0

The wet density of the high-strength concrete was 2.52gm/cc, and material property tests were conducted as part of the experimental program [6]. Concrete cylinders 12.7cm long and 6.35cm in diameter were cast for triaxial material tests. Results of the material property tests on the concrete samples are shown in Figure 4.1.2. Test data for the 48MPa concrete are included for reference. The tests were conducted in two phases: isotropic compression followed by triaxial shear. The upper plot in Figure 4.1.2 shows results from the isotropic compression phase of the experiments. Three data curves are shown for the 48MPa concrete, while results from three tests on the 140MPa concrete were simply bracketed, because the data fell too close to plot separately on this scale. Values of the maximum stress difference (or shear strength) *vs* pressure are given in the lower plot in

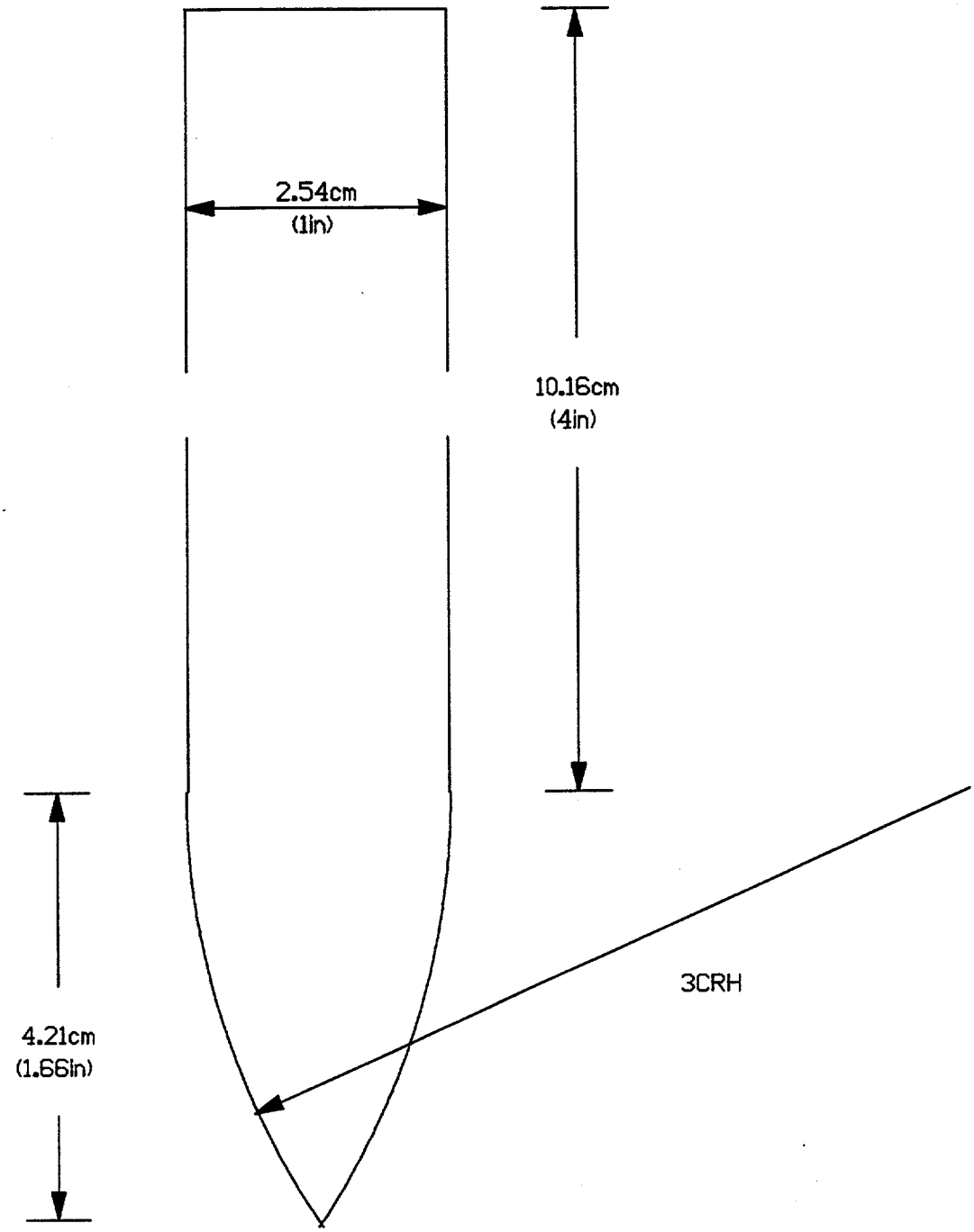

Figure 4.1.1. Projectile Geometry – Ogival-Nosed Rods for 140MPa Concrete Target Tests

Figure 4.1.2. Tensile strengths of the two concretes were measured by direct-pull tests, with the maximum unconfined tensile strength for the 140MPa concrete being ~5MPa.

4.2 CTH Model Input

The CTH calculations were performed in 2D cylindrical geometry, and Figure 4.2.1 shows the calculational setup.

Most of the calculations were performed with a basecase zoning of 75×250 cells. The x-direction mesh was started at x = 0, the axis of symmetry, and extended to a radius of 5.0cm (about four times the projectile radius), using 25 uniform cells of 0.20cm width. This was followed by 50 more cells of increasing (at ~3% rate) size in the x-direction to an outer radius of ~25cm, where a transmitting outer boundary condition was imposed. In the y-direction, the mesh was started at y = -35cm, where y = 0 was taken as the impact surface and the back surface of the target was at y = -17.8cm. Thus, a subgrid of square cells covered the penetration region, with the cell size being 0.20cm in both the x- and y-directions.

The various material properties used in the CTH calculations for this problem are given in Table 4.2.1. The penetrator and boundary layer were modelled as discussed in Section 2.2. Both the boundary layer thickness, w_{bl}, and the slip layer thickness, w_{sl}, were specified to be 0.30cm. The concrete target was modelled using the Johnson-Holmquist ceramic model [8], with material properties listed in Table 4.2.1.

As in the earlier metal penetration problems, the concrete penetration calculations were performed with the nonequilibrium, multi-material temperature and multi-material pressure modelling options, with the high-resolution interface tracker, and without the fragment mover option. Velocity was specified to be convected conserving momentum exactly and discarding any kinetic energy discrepancies. Artificial viscosity was used, with default values for the linear and quadratic coefficients, and the shear artificial viscosity increased to 0.1. The region around the penetrator and target was modelled as void.

4.3 Calculational Results

Calculations were run for six different values of impact velocity (350, 400, 500, 600, 800, and 1000 m/s). While these do not correspond exactly to any of the test conditions given in Table 4.1.1, they bracket the range of impact velocities used in the test series.

Calculated residual velocities for friction coefficients f of 0.01 and 0.10 are shown in Figure 4.3.1 as a function of impact velocity. The experimental data [6] are also shown. Generally, the calculated results and experimental data are in very good agreement. Curiously, there is little difference between calculational results for $f = 0.01$ and $f = 0.10$.

Figure 4.3.2 illustrates the shape of the penetrator and cavity predicted at four different times during the penetration process for an impact velocity of 1000m/s.

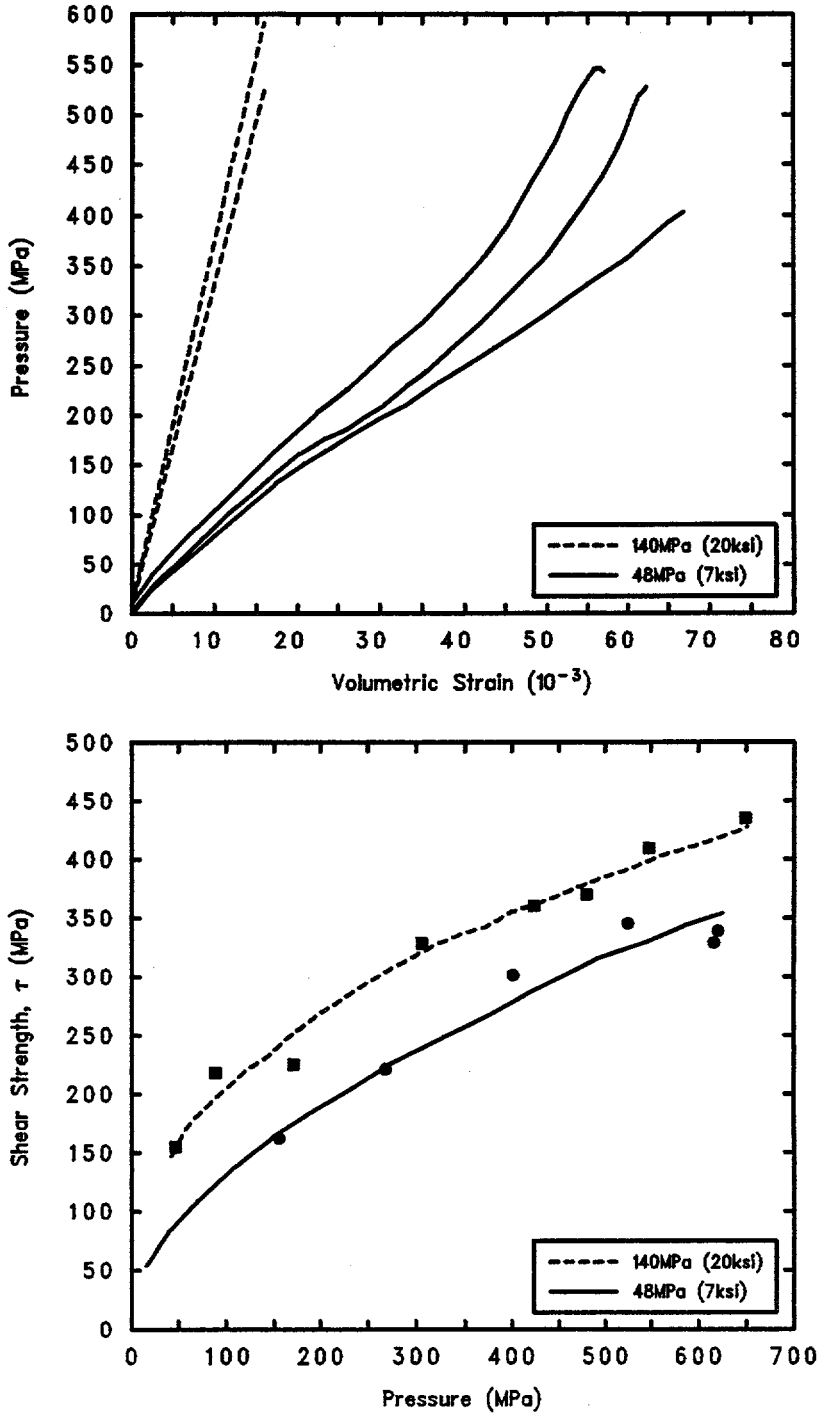

Figure 4.1.2. Materials Property Data for the 48MPa and 140MPa Concrete Target Materials

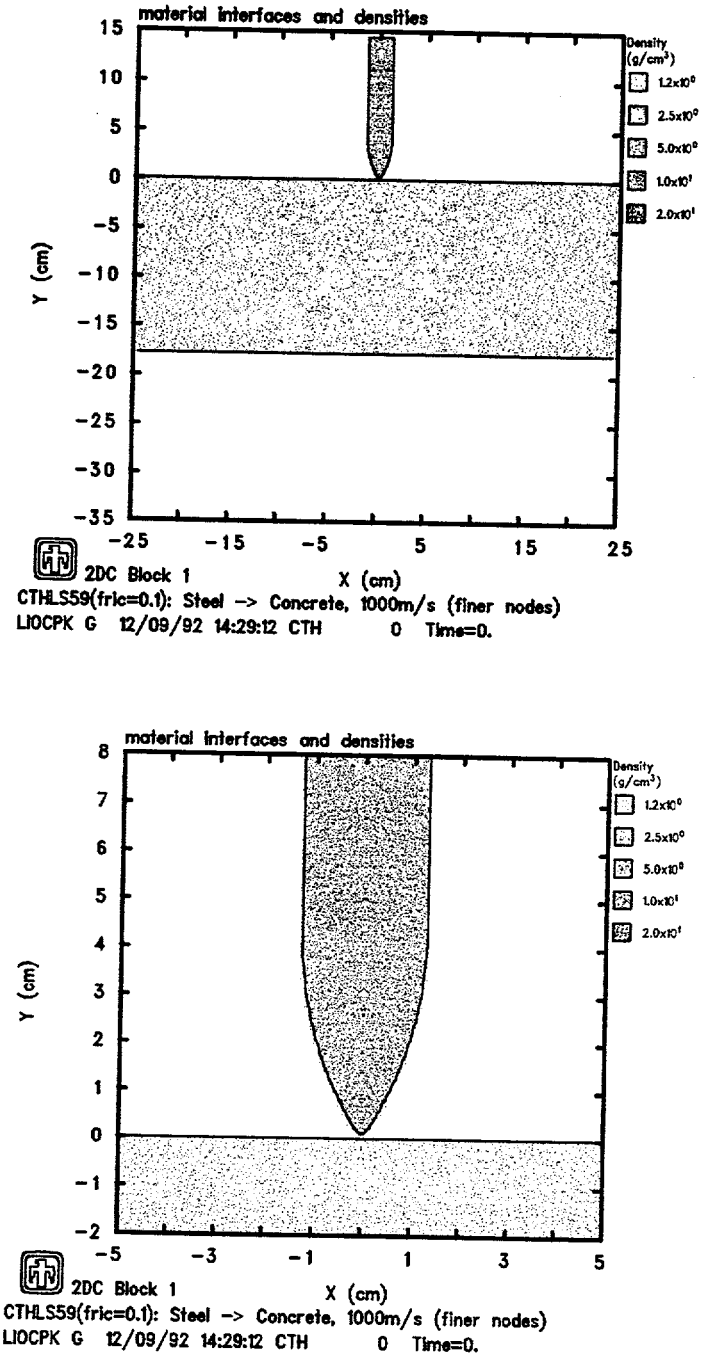

Figure 4.2.1. Initial Configuration for CTH Analyses – Ogival-Nosed Rods Penetrating 140MPa Concrete Targets

Table 4.2.1. Material Properties Used in CTH Analyses of Ogival-Nosed Rods Penetrating 140MPa Concrete Targets

Property	Penetrator (Steel)	Target (Concrete)
Density, ρ (gm/cm^3)	8.02	2.52
Sound speed, C_S (cm/s)	4.610×10^5	
$U_s - U_p$ slope, S	1.73	
Gruneisen coefficient, Γ	1.67	
Specific heat, C_V (erg/gm-eV)	5.34×10^{10}	1×10^{11}
Poisson's ratio, ν	0.3	
Yield stress, Y (dynes/cm^2)	17.2×10^9	
Johnson-Holmquist model constants		
T (dynes/cm^2)		-2×10^8
p_1 (dynes/cm^2)		1×10^9
p_2 (dynes/cm^2)		7×10^9
Y_1 (dynes/cm^2)		2×10^9
Y_2 (dynes/cm^2)		4.5×10^9
Y_3 (dynes/cm^2)		4.5×10^9
C_3 (dynes/cm^2)		1×10^{-6}
C_6 (dynes/cm^2)		0.6
ϵ^{pf*}		1×10^{99}
K_1 (dynes/cm^2)		4×10^{11}
K_2 (dynes/cm^2)		0
K_3 (dynes/cm^2)		0
β		0
$p*$ (dynes/cm^2)		0
G (dynes/cm^2)		1.25×10^{11}
P_{FRAC} (dynes/cm^2)	-35×10^9	-2×10^8

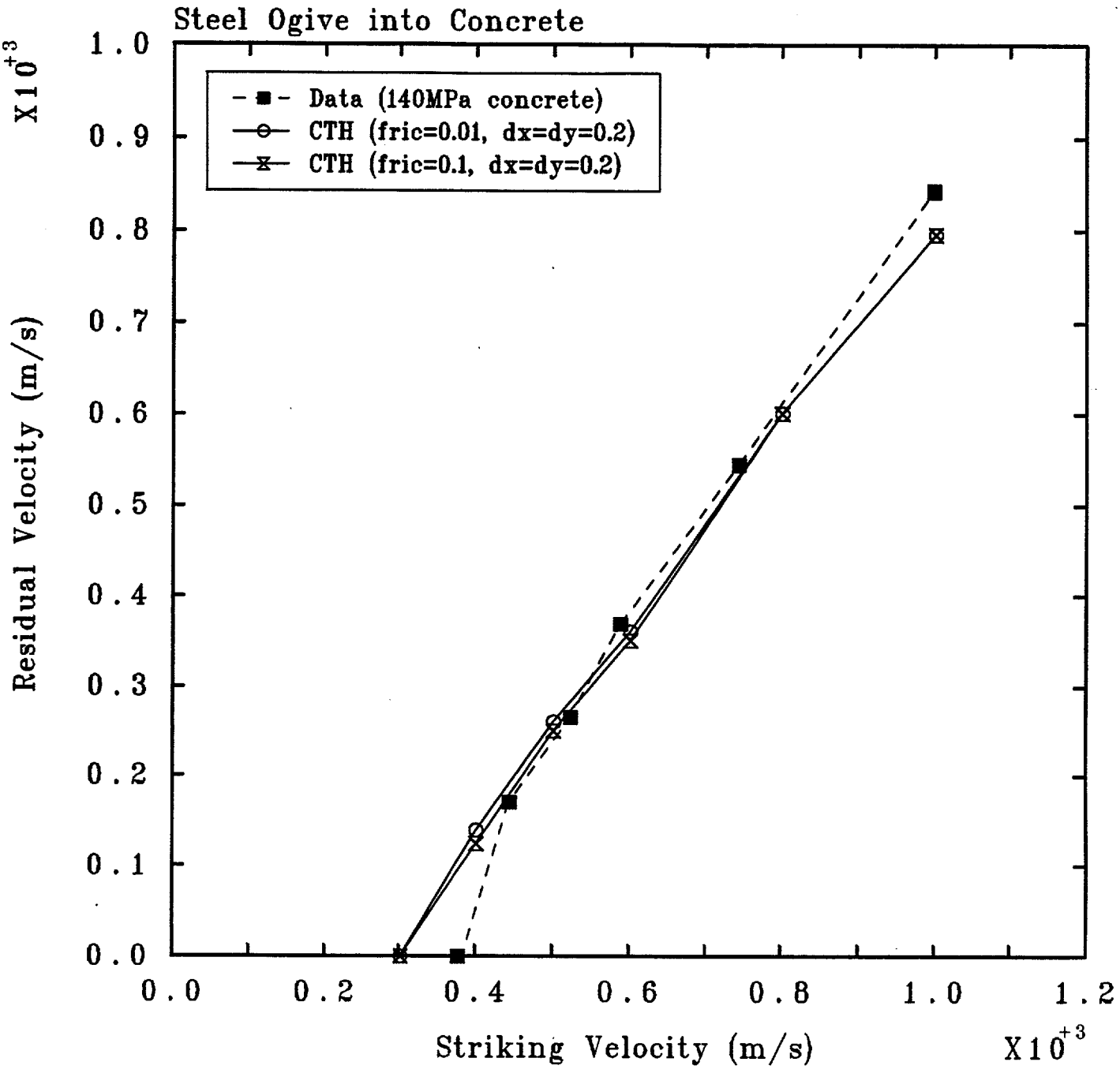

Figure 4.3.1. Residual Velocity Predicted by CTH for Various Impact Velocities and Friction Factors – Ogival-Nosed Rods Penetrating 140MPa Concrete Targets

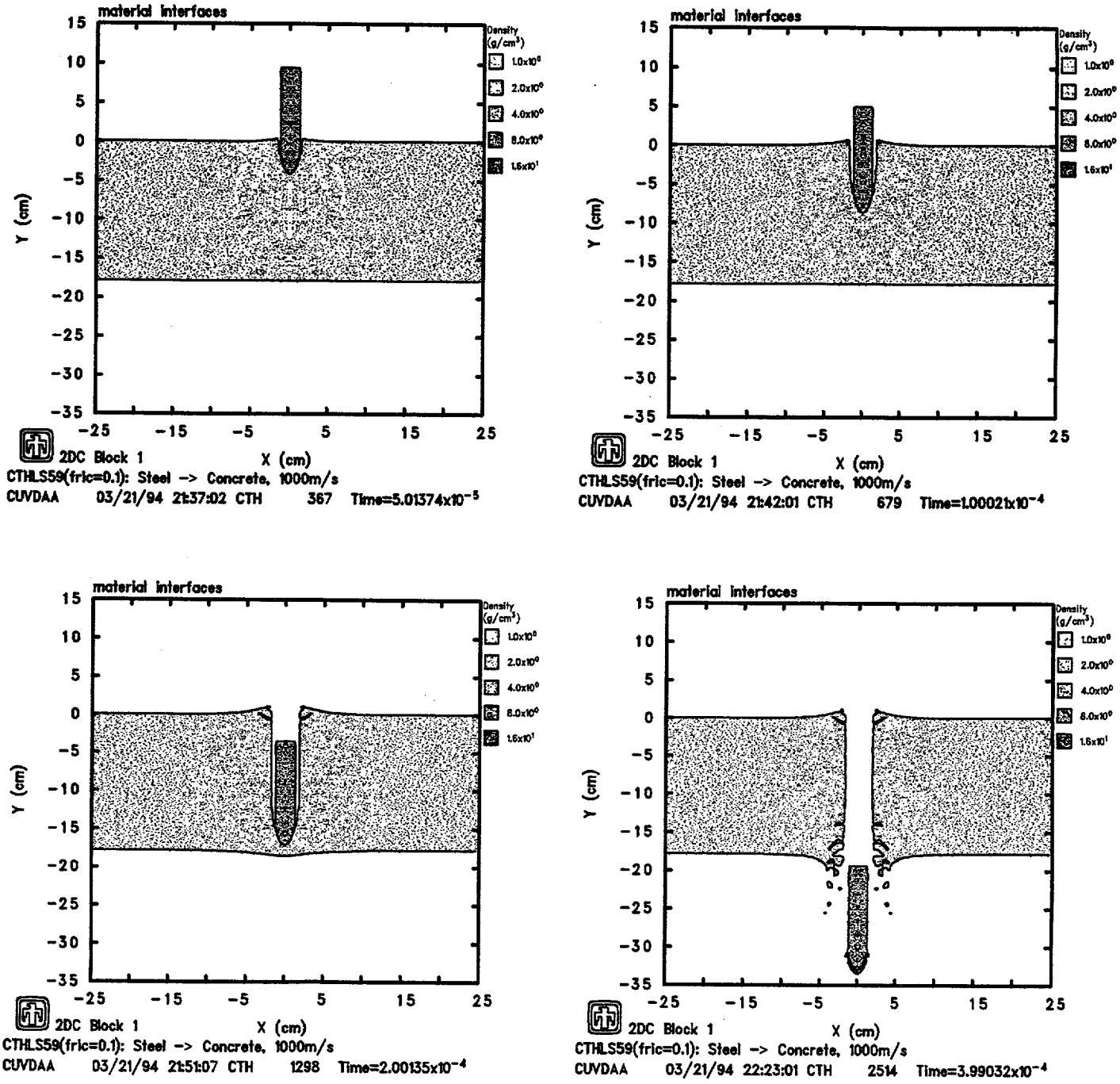

Figure 4.3.2. Penetrator and Target Configurations Predicted by CTH – Ogival-Nosed Rod Penetrating 140MPa Concrete Target at an Impact Velocity of 1000m/s

Figure 4.3.3 presents the rigid-body decelerations calculated for the various impact velocities, as a function of both velocity, in the upper plot, and depth of penetration, in the lower plot. (The rigid-body decelerations plotted in this report are the time derivatives of the mass-weighted average velocity of the penetrator material, smoothed using a bell-shaped function with a 0.05ms time constant.) For all impact velocities plotted, the decelerations between the initial rise and the final drop all fall on approximately the same deceleration *vs* velocity curve.

Calculations were done using progressively finer zoning for an impact velocity of 1000m/s with friction coefficient $f = 0.10$. In the penetration region, the zoning resolution was progressively refined by factors of 2 in each direction, to $\Delta x = \Delta y = 0.10$ and then $\Delta x = \Delta y = 0.05$, while maintaining $w_{bl} = w_{sl} = 1.5\times(\Delta x = \Delta y)$. Thus, for $\Delta x = \Delta y = 0.10$ we set $w_{bl} = w_{sl} = 0.15$, and for $\Delta x = \Delta y = 0.05$ we set $w_{bl} = w_{sl} = 0.075$. Results of the calculations are shown in Figure 4.3.4. The residual velocities calculated for this problem converge smoothly to the experimental result as the zoning is progressively refined. Figure 4.3.5 illustrates the corresponding decrease in rigid-body deceleration as the zoning resolution is improved and the associated boundary and slip layer thicknesses are decreased.

A final set of studies was done for an impact velocity of 1000m/s and the basecase zoning, in which a number of the Johnson-Holmquist material parameters used to model the concrete target were varied (see Section 4.2). The results of these sensitivity studies are shown in Figure 4.3.6. The results show little effect on residual velocity of most of the changes made. The biggest effect was seen when the limiting value of material strength (*i.e.*, Y_2) was reduced and, as would be expected, a softer concrete model resulted in a higher predicted residual velocity.

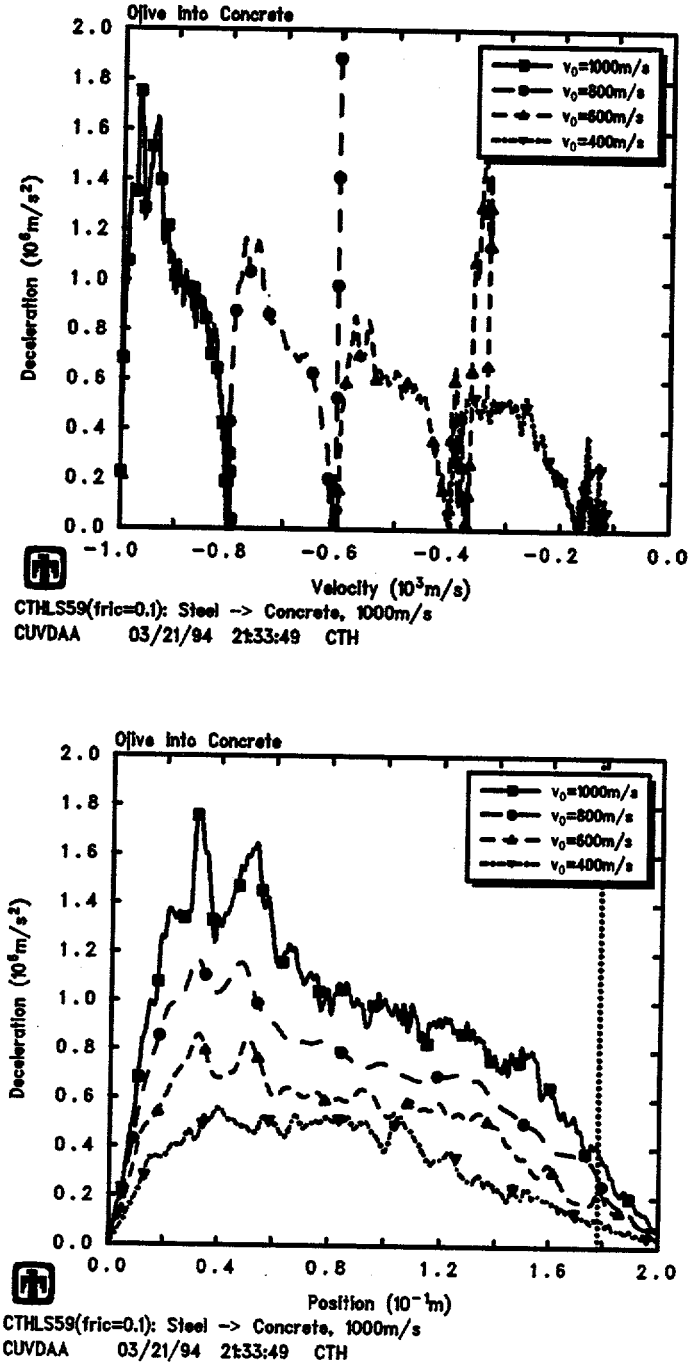

Figure 4.3.3. Rigid-Body Decelerations Predicted by CTH for Various Impact Velocities – Ogival-Nosed Rods Penetrating 140MPa Concrete Targets

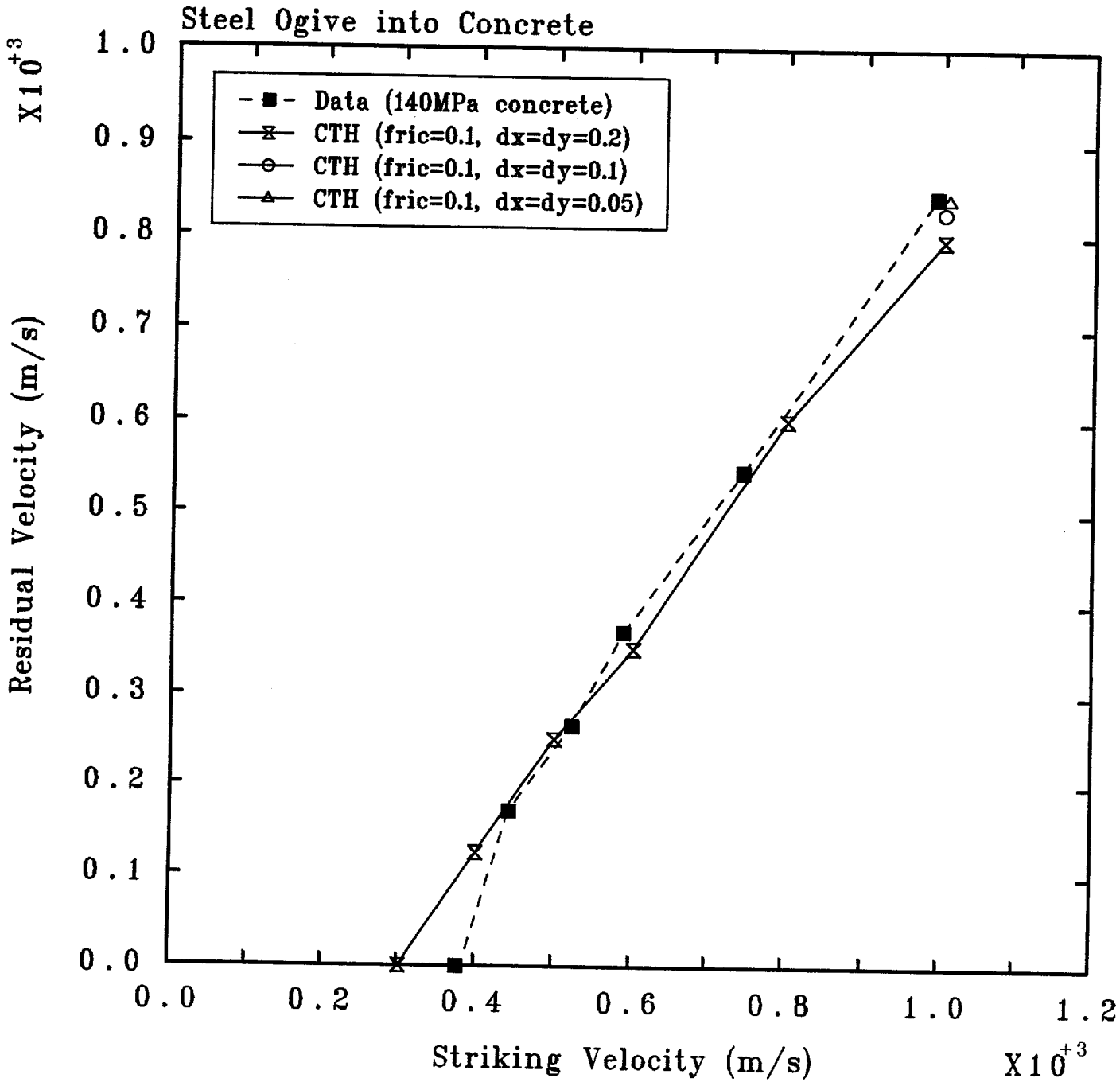

Figure 4.3.4. Residual Velocity Predicted by CTH for Various Impact Velocities and Calculational Zone Sizes – Ogival-Nosed Rods Penetrating 140MPa Concrete Targets

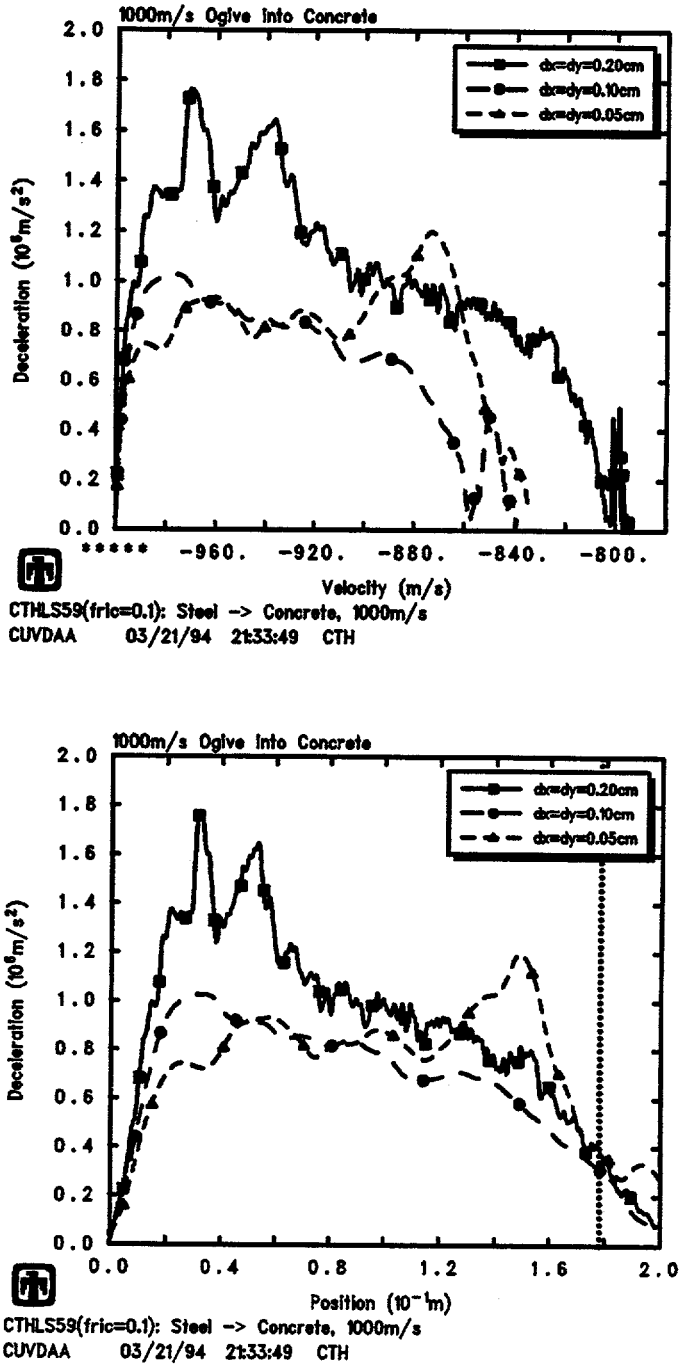

Figure 4.3.5. Rigid-Body Decelerations Predicted by CTH for an Impact Velocity of 1000m/s with Different Zone Sizes – Ogival-Nosed Rods Penetrating 140MPa Concrete Targets

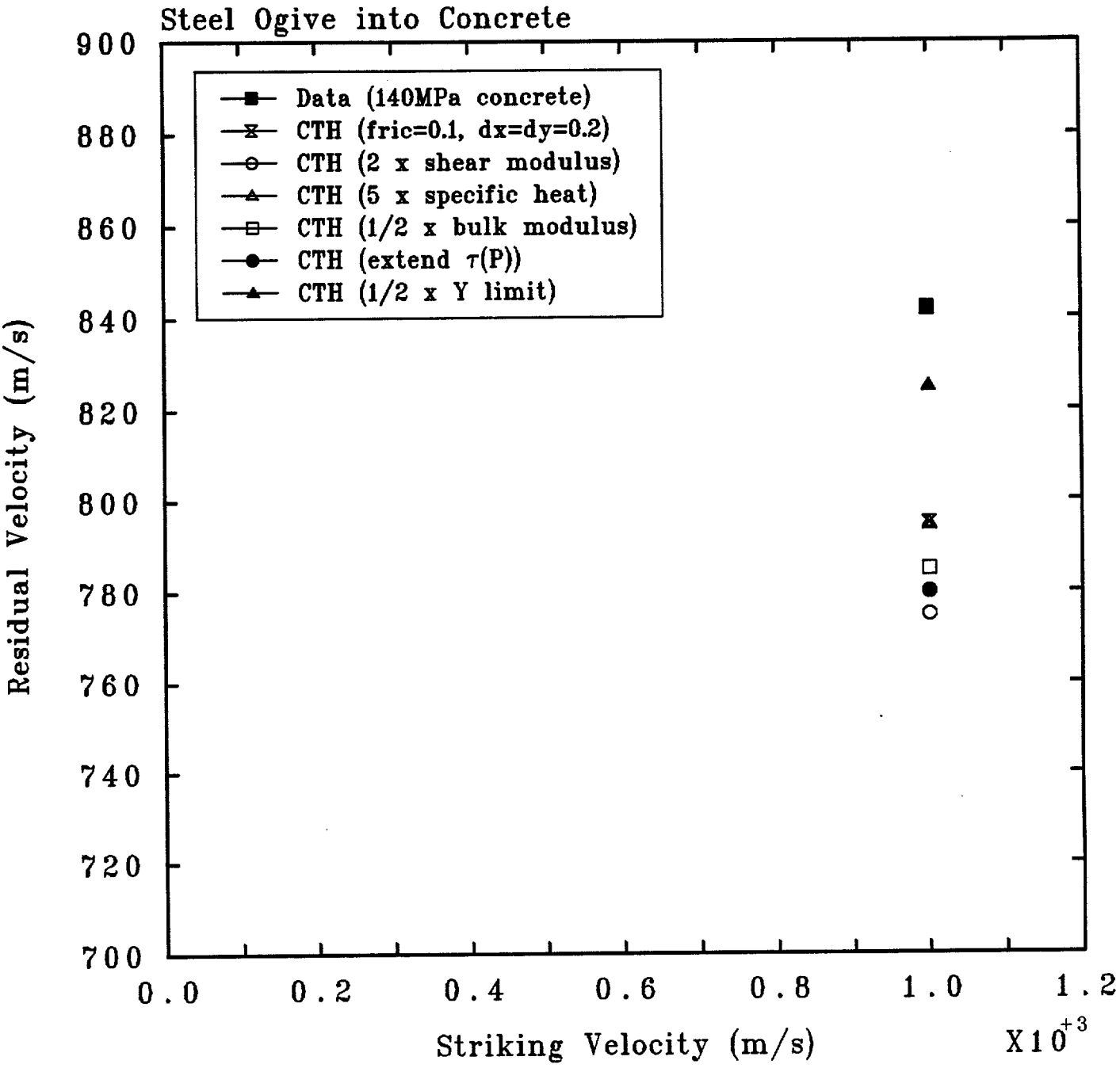

Figure 4.3.6. Residual Velocity Predicted by CTH when Concrete Material Properties are Varied – Ogival-Nosed Rods Penetrating 140MPa Concrete Targets at an Impact Velocity of 1000m/s

5 Summary and Conclusions

Two series of metal penetration experiments and a series of concrete slab perforation tests were simulated with the CTH Eulerian code. The experiments involved penetration of 7075-T651 aluminum alloy targets by ogival-nosed (3CRH) projectiles, penetration of 6061-T651 aluminum alloy targets by hemispherical-nosed rods, and penetration of unreinforced concrete slabs by ogival-nosed (3CRH) projectiles. Target material constants were determined from independent material property tests. The projectiles were made of maraging steel in all cases and impact velocities for both target types covered the range from ~300m/s to ~1200m/s. For the metal penetration experiments, depth of penetration was measured, while residual velocity of the projectile was measured for the concrete slab perforation tests. These data were compared with the CTH calculational results.

Our results demonstrate that CTH with the boundary-layer algorithm is well-suited to predict the global or "rigid-body" response of the penetrator. In all cases, the calculational results agree quite well with test data for the penetration depth or residual velocity *vs* impact velocity over the entire velocity range in the experiments. Reasonable values of friction, in the $f \sim$ 0.0-0.1 range, give calculational results which bracket the data. Friction was found to have more effect on penetration for the ogival-nosed projectiles than for the hemispherical-nosed rods.

The calculations used a new "boundary-layer" algorithm developed at Sandia to treat material interfaces in Eulerian codes. The necessity for including the boundary layer was demonstrated by results of calculations done without it, where the penetration of ogival-nosed penetrators impacting the aluminum target at high velocity was underpredicted by a factor of 2.

We also found that that the Johnson-Holmquist ceramic model gives a good representation of the concrete response for the slab penetration problems, even though it neglects some well-known features (*e.g.*, fracture, damage-induced anisotropy, porosity, *etc.*) which may be important for other problems.

Bibliography

[1] J. M. McGlaun, S. L. Thompson, L. N. Kmetyk, and M. G. Elrick, "A Brief Description of the Three-Dimensional Shock Wave Physics Code CTH", SAND89-0607, Sandia National Laboratories, July 1990.

[2] S. A. Silling, "Eulerian Simulation of the Perforation of Aluminum Plates by Nondeforming Projectiles", SAND92-0493, Sandia National Laboratories, March 1992.

[3] S. A. Silling, "CTH Reference Manual: Boundary Layer Algorithm for Sliding Interfaces in Two Dimensions", SAND93-2487, Sandia National Laboratories, January 1994.

[4] M. J. Forrestal, V. K. Luk, Z. Rosenburg, N. S. Brar, "Penetration of 7075-T651 Aluminum Targets with Ogival-Nose Rods", *Int. J. Solids Structures* **29** 14/15 (1992), 1729-1736.

[5] M. J. Forrestal, N. S. Brar, V. K. Luk, "Penetration of Stain-Hardening Targets with Rigid Spherical-Nose Rods", *J. App. Mech.* **113** (1991), 7-10.

[6] S. J. Hanchek, M. J. Forrestal, E. R. Young, J. Q. Ehrgott, "Perforation of Concrete Slabs with 48 MPa (7 ksi) and 140 MPa (20 ksi) Unconfined Compressive Strengths", *Int. J. Impact Engng.* **12** 1 (1992), 1-7.

[7] S. A. Silling, "CTH Reference Manual: Viscoplastic Models", SAND91-0292, Sandia National Laboratories, June 1991.

[8] S. A. Silling, "CTH Reference Manual: Johnson-Holmquist Ceramic Model", SAND92-0576, Sandia National Laboratories, September 1992.

A CTH Input Model for Penetration of Aluminum Targets by Ogival-Nosed Steel Rods at 1258m/s

```
*
*eor* cgenin
*
OAL2n(25kb)/CTHLS50 (6-1409): Steel -> Al, 1258 m/s
*
control
  mmp
  vis bl=0.1 bq=2. bs=0.1
endcontrol
*
mesh
  block 1  geom=2dc    type=e
      x0=0.
       x1  n=25 dxf=0.04 w=1
       x2  n=50 dxf=0.04 w=7.5
      endx
      y0=-24.0
       y1  n=825 dyl=0.04 w=33
      endy
      xaction=0 0.4
      yaction=0 9
  endb
endmesh
*
insertion of material
   block 1
     package projectile
       material 2
       numsub 50
       xvel 0.0
       yvel -1.258e5
       insert uds
         point    0.0000       0.0000
         point    0.0660       0.1061
         point    0.1256       0.2158
         point    0.1787       0.3289
         point    0.2251       0.4448
         point    0.2647       0.5633
         point    0.2972       0.6839
         point    0.3227       0.8062
         point    0.3409       0.9298
         point    0.3518       1.0542
         point    0.3555       1.1791
```

```
        point    0.3555       8.2911
        point    0.           8.2911
      endinsert
    endpackage
    package target
      material 1
      numsub 50
      xvel 0.
      yvel 0.
      insert box
        p1 0    -22.9
        p2 7.6    0
      endinsert
    endpackage
  endblock
 endinsertion
*
 edit
   block 1
   expanded
   endblock
 endedit
*
eos
  mat1 mgr r0=2.7  cs=5.380e5 s=1.337 g0=2.100 cv=1.02e11 *Al
  mat2 mgr
*    r0=8.02 cs=4.61e5 s=1.73 g0=1.67 cv=5.34e11    *Steel
    r0=9.93 cs=4.61e5 s=1.73 g0=1.67 cv=5.34e11    *Steel with density
                *increased to reflect increased effective x-sec area
endeos
*
epdata
   vpsave
   mix 3
   matep 1
     poisson 0.33
     johnson-cook 7  *7075-T651 Al
        ajo  4.48e9
        bjo  2.95e8
        njo  0.39205
        cjo  0.0
        tjo  0.0668
   matep 2 yield=31.e9 poisson=0.3   *W
   blint 1 soft 1 hard 2 wsl 0.08 wbl 0.08 fric 0
ende
*
tracer
```

```
   add 0 0.01 to 0 8.28 n 6
endt
*
*eor* cthin
*
0AL2n(25kb)/CTHLS50 (6-1409): Steel -> Al, 1258 m/s
*
restart
*  nu=2
*  time=50.e-6
endr
*
control
  mmp
  tstop = 400.0e-6
  nscycle = 150000
  rdumpf = 3600.
  ntbad=1000000
endc
*
convct
   interface=high_resolution
endc
*
edit
  shortc
    cy=0 dc=1000
  ends
  longt
    tim=1.e-6 dt=1.0
  endl
  histt
    tim=0 dtf=0.1e-6
    htracer1
    htracer2
    htracer3
    htracer4
    htracer5
    htracer6
  endh
  plott
    tim=0 dt=20.0e-6
  endp
ende
*
boundary
   bhy
```

```
     bl 1
       bxb=0 bxt=1 byb=1 byt=1
     endb
   endh
endb
*
fracts
  pressure
  pfrac1 -5.0e9 *Al
  pfrac2 -35.0e9 *Steel
endf
*
```

B CTH Input Model for Penetration of Aluminum Targets by Hemispherical-Nosed Steel Rods at 1009m/s

```
*
*eor* cgenin
*
Shot No 1912: Steel -> Al, 1009 m/s, fric=0
*
control
  mmp
  vis bl=0.1 bq=2. bs=0.1
endcontrol
*
mesh
  block 1  geom=2dc    type=e
       x0=0.
        x1  n=25 dxf=0.04 w=1
        x2  n=50 dxf=0.04 w=7.5
       endx
       y0=-24
        y1  dyf=0.04 dyl=0.04 w=32
*       y0=-13.0
*        y1  n=550 dyl=0.04 w=22
       endy
       xaction=0 0.4
       yaction=0 9
  endb
endmesh
*
insertion of material
   block 1
     package projectile
       material 2
       numsub 50
       xvel 0.0
       yvel -1.009e5
       insert box
         p1 0 0.3555 p2 0.3555 7.1476
       endinsert
     endpackage
     package projectile
       material 2
       numsub 50
       xvel 0.0
       yvel -1.009e5
```

```
      insert circle
        cen 0 0.3555 rad 0.3555
      endinsert
    endpackage
    package target
      material 1
      numsub 50
      xvel 0.
      yvel 0.
      insert box
        p1 0    -21.6
        p2 7.6    0
      endinsert
    endpackage
  endblock
 endinsertion
*
 edit
  block 1
  expanded
  endblock
 endedit
*
eos
  mat1 mgr r0=2.7  cs=5.380e5 s=1.337 g0=2.100 cv=1.02e11 *Al
  mat2 mgr
*    r0=8.02 cs=4.61e5 s=1.73 g0=1.67 cv=5.34e11    *Steel
    r0=9.93 cs=4.61e5 s=1.73 g0=1.67 cv=5.34e11    *Steel with density
                *increased to reflect increased effective x-sec area
endeos
*
epdata
  vpsave
  mix 3
  matep 1
    poisson 0.33
    johnson-cook user  *6061-T651 Al from experimental sample
       ajo  2.76e9
       bjo  0.92e9
       njo  0.2591
       cjo  0.0
       mjo  1.0
       tjo  0.0959
  *matep 2 yield=25.e9 poisson=0.3   *steel
  matep 2 yield=31.e9 poisson=0.3   *steel with scaling for x-sec area
  blint 1 soft 1 hard 2 wsl 0.08 wbl 0.08 fric 0
ende
```

```
*
tracer
   add 0 0.3555 to 0 8.1 n 6
   add 5 -5
endt
*
*eor* cthin
*
Shot No 1912: Steel -> Al, 1009 m/s, fric=0
*
restart
*  nu=2
*  time=50.e-6
endr
*
control
  mmp
  tstop = 400.0e-6
  nscycle = 150000
  rdumpf = 3600.
  ntbad=1000000
endc
*
convct
   interface=high_resolution
endc
*
edit
  shortc
    cy=0 dc=1000
  ends
  longt
    tim=1.e-6 dt=1.0
  endl
  histt
    tim=0 dtf=0.25e-6
    htracer1
    htracer2
    htracer3
    htracer4
    htracer5
    htracer6
  endh
  plott
    tim=0 dt=50.0e-6
  endp
ende
```

```
*
fragment
  mat 1
  ntracer 7
  dcycle 50
endf
*
boundary
   bhy
     bl 1
       bxb=0 bxt=1 byb=1 byt=1
     endb
   endh
endb
*
fracts
  pressure
  pfrac1 -10.0e9 *Al
  pfrac2 -35.0e9 *Steel
endf
*
```

C CTH Input Model for Penetration of Concrete Targets by Ogival-Nosed Steel Rods at 1000m/s

```
*
*eor* cgenin
*
CTHLS59: Steel -> Concrete, 1000m/s
*
control
  mmp
  vis bl=0.1 bq=2. bs=0.1
endcontrol
*
mesh
  block 1  geom=2dc    type=e
      x0=0.
       x1  n=25 dxf=0.20 w=5.0
       x2  n=50 dxf=0.20 w=20.0
      endx
      y0=-35.0
       y1  n=250 dyl=0.20 w=50.0
      endy
      xaction=0 1.3
      yaction=0 15.0
  endb
endmesh
*
insertion of material
   block 1
     package projectile
       material 2
       numsub 50
       xvel 0.0
       yvel -1.00e5
       insert box
         x1  0.0    x2   1.27
         y1  4.21   y2  14.37
       endinsert
     endpackage
     package projectile
       material 2
       numsub 50
       xvel 0.0
       yvel -1.00e5
       insert circle
         center  -6.35  4.21
```

```
        radius   7.62
      endinsert
      delete box
        x1  0.0    x2  99.99
        y1  4.21   y2  99.99
      enddelete
      delete box
        x1  0.0    x2  99.99
        y1  -99.   y2   0.00
      enddelete
    endpackage
    package target
      material 1
      numsub 50
      xvel 0.
      yvel 0.
      insert box
        p1 0    -17.8
        p2 99.9   0
      endinsert
    endpackage
  endblock
 endinsertion
*
 edit
   block 1
   expanded
   endblock
 endedit
*
eos
  mat1 jhcer
    jht=-2.0e8  jhp1=1.0e9  jhp2=7.0e9  jhc6=0.6  jhc3=1.0e-6
    jhs1=2.0e9  jhs2=4.5e9  jhs3=4.5e9  jhbeta=0.0  jhrho=2.52
    jhdp1=0.0  jhefmax=1.0e99  jhk1=4.0e11  jhk2=0.0  jhk3=0.0
    jhcv=1.0e11  jhshrm=1.25e11  *  concrete
  mat2 mgr
*    r0=8.02 cs=4.61e5 s=1.73 g0=1.67 cv=5.34e11    *Steel
    r0=10.0 cs=4.61e5 s=1.73 g0=1.67 cv=5.34e11    *Steel with density
                  *increased to reflect increased effective x-sec area
endeos
*
epdata
   vpsave
   mix 3
   matep 1  jhcer
   matep 2 yield=21.5e9 poisson=0.3   *W
```

```
   blint 1 soft 1 hard 2 wsl 0.30 wbl 0.30 fric 0.01
ende
*
tracer
   add 0 0.01 to 0 14.35 n 9
endt
*
*eor* cthin
*
CTHLS59: Steel -> Concrete, 1000m/s
*
control
  mmp
  tstop = 399.0e-6
  nscycle = 150000
  rdumpf = 3600.
  ntbad=1000000
endc
*
convct
   interface=high_resolution
endc
*
edit
  shortc
    cy=0 dc=1000
  ends
  longt
    tim=1.e-6 dt=1.0
  endl
  histt
    tim=0 dtf=0.1e-6
    htracer1
    htracer2
    htracer3
    htracer4
    htracer5
    htracer6
  endh
  plott
    tim=0 dt=25.0e-6
  endp
ende
*
boundary
   bhy
     bl 1
```

```
        bxb=0 bxt=1 byb=1 byt=1
      endb
    endh
endb
*
fracts
  pressure
  pfrac1 -2.0e8 *Al
  pfrac2 -35.0e9 *Steel
endf
*
```

Report Distribution List:

M. D. Adley
U. S. Army Engineers
Waterways Experiment Station
Concrete Technology Division
3909 Halls Ferry Road
Vicksburg, MI 39180-6199

F. Allahdadi
Phillips Laboratory
PL/WSSD
Kirtland AFB, NM 87117-6008

Southwest Research Institute (2)
P.O. Drawer 28510
San Antonio, TX 78228-0510
Attn: C. E. Anderson & J. D. Walker

Barry L. Bingham
Applied Research Associates, Inc.
4300 San Mateo Blvd. NE
Suite A220
Albuquerque, NM 87110

U. S. Army ARDEC (2)
SMCAR-AEE-WW, Bldg. 3022
Picatinny Arsenal, NJ 07806-5000
Attn: C. Chin & E. Baker

Lockheed Missiles and Space Company (2)
Organization 89-10, Bldg. 157
P. O. Box 3504
Sunnyvale, CA 94088-3504
Attn: Y. Choo & E. Matheson

Dwight Clark
Thiokol Corporation
Science & Engineering Division
P. O. Box 707, Mailstop 280
Brigham City, Utah 84302-0707

Wright Laboratory (3)
WL/MNMW, Bldg. 13
Eglin AFB, FL 32542-5434
Attn: J. Collins, M. Nixon, J. C. Foster

R. Hunt
Wright Laboratory
WL/MNSA
Eglin AFB, FL 32542-5434

Gordon R. Johnson
Alliant Techsystems Inc.
600 2nd Street NE (MN11-2925)
Hopkins, MN 55343

U. S. Army Research Laboratory (7)
AMSRL-WT-TC
Aberdeen Proving Ground MD 21005-5066
Attn: K. Kimsey, H. Meyer, G. Randers-Pehrson, J. Dehn,
Y. Huang, D. Scheffler, S. Segletes,

Eric Lundstrom
Naval Air Warfare Center
Weapons Division, Code 3261
China Lake, CA 93555

Naval Surface Warfare Center (3)
Code R14
10901 New Hampshire Ave.
Silver Spring, MD 20903-5000
Attn: H. Mair, W. Reed, & P. Walters

Charles E. Needham
Maxwell/S-CUBED
2501 Yale SE
Suite 300
Albuquerque, NM 87106

Maj. William Oliver
U. S. Army Medical Corp
Armed Forces Institute of Pathology
Department of Cellular Biology
Washington, DC 20306-6000

D.L. Orphal
California Research & Technology, Inc.
5117 Johnson Dr.
Pleasanton, CA 94588

P. F. Radkowski, III
Radkowski Associates
P. O. Box 1121
Los Alamos, NM 87544

Teledyne Brown Engineering (2)
300 Sparkman Drive, MS/50
P. O. Box 070007
Huntsville, AL 35807-7007
Attn: B. Loper, M. White

Guy Spitale
Jet Propulsion Laboratory
California Institute of Technology
Reliability Engineering Section
4800 Oak Grove Drive
Pasadena, CA 91109

Los Alamos National Laboratory
Mail Station 5000
P.O. Box 1663
Los Alamos, NM 87545
Attn: T. F. Adams, MS F663
Attn: S. T. Bennion, MS F663
Attn: W. Birchler, MS J576
Attn: M. W. Burkett, MS G787
Attn: E. J. Chapyak, MS F663
Attn: D. Mandell, MS F663

University of California
Lawrence Livermore National Laboratory
7000 East Ave.
P.O. Box 808
Livermore, CA 94550
Attn: M. J. Murphy, MS L-368
Attn: J. E. Reaugh, MS L-290
Attn: D. J. Steinberg, MS L-35
Attn: R. E. Tipton, MS L-35

Sandia National Laboratories

0321 E. H. Barsis (1400)
0819 J. M. McGlaun (1431)
0819 K. G. Budge (1431)
0819 M. G. Elrick (1431)
0819 E. S. Hertel (1431)
1393 R. J. Lawrence (5609)
0819 J. S. Peery (1431)
0819 S. V. Petney (1431)
0819 A. C. Robinson (1431)
0819 T. G. Trucano (1431)
0820 P. Yarrington (1432) (10)
0820 R. L. Bell (1432)
0820 R. M. Brannon(1432)
0820 P. J. Chen (1432)
0820 H. E. Fang (1432)
0820 A. V. Farnsworth (1432)
0820 G. I. Kerley (1432)
0820 M. E. Kipp (1432)
0820 F. R. Norwood (1432)
0820 S. A. Silling (1432)
0820 P. A. Taylor (1432)
0821 P. L. Stanton (1433)
0821 J. A. Ang (1404)
0821 L. C. Chhabildas (1433)
0821 M. D. Furnish (1433)
0821 D. E. Grady (1433)
0437 J. W. Swegle (1562)
0100 Document Processing DOE/OSTI (7613-2) (10)
0745 S. L. Thompson (6418)
0745 L. N. Kmetyk (6418) (10)
0899 Technical Library (13414) (7)
0619 Technical Publications (13416)
9018 Central Technical Files (8523-2)
9042 G. A. Benedetti (8741)
9042 M. L. Chiesa (8741)
9042 L. E. Voelker (8741)
8742 J. J. Dike (8742)
9042 A. McDonald (8742)
9042 V. D. Revelli (8742)
9042 L. I. Weingarten (8742)
9043 M. L. Callabresi (8743)
9043 D. J. Bammann (8743)
0303 R. O. Nellums (9722)
0303 M. J. Forrestal (9723)
0303 J. T. Hitchcock (9723)